Spectroscopic signatures of youth in low-mass kinematic candidates of young moving groups

M. C. Gálvez-Ortiz,[1,2]★ M. Kuznetsov,[3,4] J. R. A. Clarke,[2] Ya. V. Pavlenko,[2,3]
S. L. Folkes,[2,5] D. J. Pinfield,[2] H. R. A. Jones,[2] J. S. Jenkins,[2,6] J. R. Barnes,[2]
B. Burningham,[2] A. C. Day-Jones,[2,6] E. L. Martín,[1] A. E. García Pérez,[7]
C. del Burgo[4] and R. S. Pokorny[8]

[1]*Centro de Astrobiología (CSIC-INTA), Crta, Ajalvil km 4, E-28850 Torrejón de Ardoz, Madrid, Spain*
[2]*Centre for Astrophysics Research, Science and Technology Research Institute, University of Hertfordshire, Hatfield AL10 9AB, UK*
[3]*Main Astronomical Observatory, Academy of Sciences of Ukraine, Golosiiv Woods, Kyiv-127, UA-03680, Ukraine*
[4]*Instituto Nacional de Astrofísica, Óptica y Electrónica (INAOE), Luis Enrique Erro 1, Sta. Ma. Tonantzintla, Puebla 72840, Mexico*
[5]*Departamento de Física y Astronomía, Facultad de ciencias, Universidad de Valparaíso, Ave. Gran Bretaña 1111, Playa Ancha, Casilla 53, Valparaíso, Chile*
[6]*Department of Astronomy, Universidad de Chile, Casilla Postal 36D, Santiago, Chile*
[7]*Department of Astronomy, University of Virginia, PO Box 400325, Charlottesville, VA 22904-4325, USA*
[8]*Yunnan Observatory, PO Box 110, CAS, 650011 Kunming, P. R. China*

ABSTRACT

We present a study of age-related spectral signatures observed in 25 young low-mass objects that we have previously determined as possible kinematic members of five young moving groups: the Local Association (Pleiades moving group, age = 20–150 Myr), the Ursa Major group (Sirius supercluster, age = 300 Myr), the Hyades supercluster (age = 600 Myr), IC 2391 supercluster (age = 35–55 Myr) and the Castor moving group (age = 200 Myr). In this paper we characterize the spectral properties of observed high- or low-resolution spectra of our kinematic members by fitting theoretical spectral distributions. We study signatures of youth, such as lithium I 6708Å, Hα emission and other age-sensitive spectroscopic signatures in order to confirm the kinematic memberships through age constraints. We find that 21 (84 per cent) targets show spectroscopic signatures of youth in agreement with the age ranges of the moving group to which membership is implied. For two further objects, age-related constraints remain difficult to determine from our analysis. In addition, we confirm two moving group kinematic candidates as brown dwarfs.

Key words: brown dwarfs – stars: kinematics and dynamics – stars: low-mass.

1 INTRODUCTION

Identifying members of known moving groups (MG) or open clusters can provide an important constraint on their age and composition. Low-mass stars and brown dwarf (BD) members of known MGs or open clusters can provide important feedback to atmospheric and evolutionary models of such objects at young ages, which currently await good calibration from constraints on age and composition. Therefore, there exists the requirement of compiling a sample of MG members in this mass range that can be used as anchor points or test-beds for these models.

In this paper we present the last in a series of results of a major survey of Ultra-Cool Dwarfs (UCDs; objects with a spectral clas-

sification of M7 or later corresponding to $T_{\rm eff}$ <2500 K), in young MGs which began with the results presented in Clarke et al. (2010, hereafter Paper I) and Gálvez-Ortiz et al. (2010, hereafter Paper II). We focus here on the study of age-sensitive spectroscopic signatures such as gravity-sensitive features (e.g. Gorlova et al. 2003; McGovern et al. 2004), Hα emission (e.g. West et al. 2004, 2008, 2011) and the presence of Li I 6708Å in a sample of objects previously classified as members of a MG based on kinematic or astrometric criteria.

Despite the recent disagreement about the origin of MGs (Famaey et al. 2007; Antoja et al. 2008; Famaey, Siebert & Jorissen 2008; Klement, Fuchs & Rix 2008; Francis & Anderson 2009; Zhao, Zhao & Chen 2009; López-Santiago, Micela & Montes 2009; Bovy & Hogg 2010; Murgas et al. 2013), and as we discussed in Paper II, we are assuming the classical concept: a MG is a young stellar population that shares a common space motion (e.g. Pinfield et al. 2006)

★ E-mail: mcz@cab.inta-csic.es

whose members have a common origin, and therefore, age and composition. We focused our studies on well-documented groups: the Hyades supercluster (HY; 600 Myr), the Ursa Major group (Sirius supercluster) (Si; 300 Myr), IC 2391 supercluster (IC; 35–55 Myr), the Castor Moving Group (CA; 200 Myr), and the Local Association (20–150 Myr) or Pleiades (PL) MG (see Papers I and II for details of MG properties and references thereof).

Many efforts have been made to obtain accurate models to understand the cool and complex atmospheres of low mass stellar and substellar objects (e.g. Kirkpatrick et al. 1993; Rajpurohit et al. 2011, 2012; Reylé et al. 2011). But the models still show discrepancies, for example in the strength of some absorption bands: discrepancies likely due to inaccurate atomic parameters and/or missing molecular opacities. Also, dust formation and its behaviour with temperature change spectral characteristics in many ways. Models that describe Very Low-Mass stars (VLMS) and BD atmospheres cannot hope to be in agreement with observations without the inclusion of dust. The onset of iron and silicate dust grain formation suspended in the photospheres of late-type M dwarfs through the L dwarf spectral sub-types is accompanied by spectral reddening, especially in near-IR (based upon the size, quantity and distribution of this dust). The T dwarf spectral sub-type sequence demonstrates a reversal to bluer colours due to the dust settling below the photosphere, thus reducing the reddening. Consequently, atmospheric models that describe dwarf objects with $T_{\rm eff} \leq 2800$ K should include treatment for the effects of atmospheric dust evolution.

Up to date, there are several families of stellar model atmospheres of VLMSs. These models are still incomplete or approximate in some physical properties (opacities, oscillator strengths for some lines and molecular bands, etc.), showing few or considerable discrepancies depending on the atmospheric regions, temperatures, etc., and there are also non-covered areas or 'gaps'. A comprehensive study of models tested by observations is needed to fully understand this cool atmosphere. Since BDs are objects occupying an intermediate position between stars and giant planets, studying their atmospheres can help us to better understand the processes in giant exo-planet atmospheres. The determination of the physical properties of VLMS and BDs is also important for understanding a broad range of topics including stellar and planetary formation, circumstellar discs, dust formation in cool atmospheres, and the initial mass function.

By comparing high- and low-resolution optical spectra of our 25 low-mass stars and BD kinematic MG candidates with a grid of atmospheric models, we can obtain effective temperature and surface gravity estimates.

In Section 2 we describe the sample characteristics and selection criteria, while in Section 3 we present details of our observations and data reduction techniques. In Section 4 we explain the model atmosphere fitting process, and in Section 5 we describe the age indicators and the analysis used to assess the sample memberships. Finally, in Section 6 we present a brief discussion and summary of our results.

2 SAMPLE

We present here the study of two different samples.

2.1 Sample A

We used photometric and astrometric criteria to combine an extended version of the Liverpool-Edinburgh High Proper Motion survey (ELEHPM; Pokorny, Jones & Hambly 2003; Pokorny et al. 2004) and Southern Infrared Proper Motion Survey (SIPS; Deacon, Hambly & Cooke 2005; Deacon & Hambly 2007) with the Two Micron All Sky Survey (2MASS), and applied colour cuts of $J - K_{\rm s} \geq 1.0$ and $R - K_{\rm s} \geq 5.0$ to select objects with spectral type predominantly later than M6V. To these we applied proper motion restriction, $\mu/\Delta\sigma_\mu > 4$ (μ is proper motion and σ_μ is the proper motion one sigma uncertainty), to ensure a 4σ level of proper motion accuracy before searching for stars with proper motions consistent with any of the MGs. Of the 817 red object catalogue we obtained by using both astrometric and photometric criteria, we concluded that 132 of these objects were possible members of one or more of the five MGs in the study (see Paper I for details).

From this sample we then obtained high-resolution spectra of 68 objects with spectral types ranging M4.5-L1. Using these high-resolution spectra we derived Galactic space–velocity components and applied a simple kinematic criterion. We found that 49 targets have kinematics consistent with the young disc population (YD; see e.g. Eggen 1984a,b, 1989) and that 36 of them possibly belong to one of the five MGs in this study. We also measured (where possible) projected rotational velocities and used the rotation rate as a supporting criterion of youth in confirming the kinematic members. We found that 31 young disc candidates have moderately high rotational velocities which also suggest youth and that 12 others have significantly high rotations to consider for further investigation as possible young stars (see Paper II for details).

We present here high-resolution follow-up observations for the 13 brightest stars in this sample, which we took in order to use other spectroscopic age criteria to confirm kinematic membership. In Table 1 we give the name, coordinates, 2MASS J magnitude and the MG candidature assigned from the kinematic study and the rotational velocities obtained in Paper II.

2.2 Sample B

Our second sample consists of objects selected from the catalogue of Folkes et al. (2012), and the reader is referred to this publication for full details of the selection method used in the creation of the catalogue. These authors present a UCD catalogue containing 245 objects with spectral types of late-M through to the L–T transition from low southern Galactic latitudes, in an area covering 5042 deg^2 within $220° \leq l \leq 260°$ and $0° \leq l \leq 60°$ for $|b| \leq 15°$, identified as part of a deep search using 2MASS near-IR and SuperCOSMOS optical photometry selection criteria as well as reduced proper motion constraints.

2.2.1 UCD sample selection procedure

(i) Photometry: using an optimal set of optical/near-IR selection criteria for the $(J - H)/(J - K_{\rm s})$ two-colour plane along with optical/near-IR colours of $(B_J - K_{\rm s})$, $(R_c - K_{\rm s})$, $(I_c - K_{\rm s})$ and the optical colour of $(R - I)_c$, with $JHK_{\rm s}$ from 2MASS, we obtained a sample of objects in the spectral range of ∼M8V to ∼L9. The selection method also included an R_F and I_N photometric surface gravity test with additional photometric constraints [see figs 1–3, and section 2 of Folkes et al. (2012) for details].

(ii) Astrometry: to eliminate bright distant contaminants, which one would expect to display small proper motions, a reduced proper motion diagram was used to segregate giant from dwarfs (e.g. Luyten 1978). In this case we used a diagram of reduced proper motion in 2MASS $K_{\rm s}$ band plotted against $(V - K_{\rm s})$ colour [see fig. 6 and section 2.5 of Folkes et al. (2012) for details].

Table 1. A: Properties for sample A.

Name	α (2000) (h m s)	δ (2000) ($\circ\,'\,''$)	*J*-mag	Moving group[1] candidature	$V\sin i$[2] (km s^{-1})
SIPS0007−2458	0 7 7.800	−24 58 3.80	13.11 ± 0.02	IC	18
2MASS0020−2346	0 20 23.155	23 46 5.38	12.35 ± 0.02	YD	12
DENIS0021−4244	0 21 5.896	−42 44 43.33	13.52 ± 0.03	IC, CA	11
SIPS0027−5401	0 27 23.240	54 1 46.20	12.36 ± 0.02	HY	27
SIPS0153−5122	1 53 11.430	51 22 24.99	13.45 ± 0.03	IC, HY	14
SIPS0214−3237	2 14 45.440	−32 37 58.20	14.01 ± 0.02	HY	18
SIPS0235−0711	2 35 49.470	7 11 21.90	12.45 ± 0.03	HY	22
2MASS0334−2130	3 34 10.657	21 30 34.35	11.91 ± 0.02	IC	<10[a]
SIPS2039−1126	20 39 13.081	−11 26 52.30	13.79 ± 0.03	PL	>15
SIPS2045−6332	20 45 2.278	−63 32 5.30	12.62 ± 0.03	PL, CA	>15
LEHPM4908	22 36 42.656	−69 34 59.30	12.68 ± 0.02	HY	−
2MASS2254−3228	22 54 58.110	32 28 52.20	13.58 ± 0.03	PL, CA	19
LEHPM6542	23 57 54.822	19 55 1.89	13.31 ± 0.02	HY	16

[1]MG to which targets are kinematic candidate (Paper II). HY = Hyades MG; SI = Ursa Major group;
CA = Castor MG; PL = Pleiades; IC = IC 2391 MG; YD = Other young disc object.
[2]From Paper II.
[a]Measured with low S/N.

2.2.2 MG selection procedure

To find possible MG members from this UCD sample, Folkes (2009) applied the astrometric and photometric test described in sections 3.2 and 3.3 of Paper I (used in the selection process of sample A.) Spectral types and photometric distances were derived from the $(I − J)$ colour using the $M_J/(I_C − J)$, and M_J/SpT relations of Dahn et al. (2002).

From these photometric and astrometric criteria Folkes (2009) identified 23 objects, with spectral types ranging from M3 to L0 as possible MG members, from which we could observe 12 that form sample B.

Here we obtain spectral classification and confirm (or otherwise) the youth of these candidates, through low-resolution spectroscopy and by studying age-sensitive spectral features. In Table 2 we give the name, coordinates, 2MASS *J* magnitude and the MG candidature assignation.

2.2.3 Spectral type determination

To improve the previous photometric spectral-type determination from Folkes (2009), we calculated a variety of different spectroscopic indices: PC3, TiO1+TiO2 and VO1+VO2 from Martín et al. (1999); The VO index from Kirkpatrick, Henry & Simons (1995);

VO-a and TiO5 from Cruz & Reid (2002). Since the TiO1+TiO2 and VO1+VO2 indices can imply two different spectral types (see fig. 9 of Martín et al. 1999), we only considered them if they were consistent with the spectral types obtained by the other indices. From these a mean spectral type was calculated.

Some objects show considerable discrepancies between spectral type derived from photometry and that from spectroscopic indices. That is, with the exception of two objects (2MASS1756−4518 and 2MASS1909−1937) with very similar photometric and spectroscopic spectral classifications. This difference is marked by the systematic assignment of a later spectral type by the photometric method. Also the difference between the two classifications appears greater for redder objects. Even with care during selection, the objects of sample B are situated in highly populated and reddened areas within the photometric selection planes, which could have produced these differences. Also, the possible presence of dust in these atmospheres could account for redder colours, therefore suggesting later spectral types. We used the spectral types derived from spectroscopy for all calculations.

3 OBSERVATIONS

For this paper we analysed optical high-resolution echelle spectra of 13 objects (sample A; Table 1) and low-resolution long slit spectra

Table 2. B: Properties for sample B.

Name	α (2000) (h m s)	δ (2000) ($\circ\,'\,''$)	*J*-mag	Moving group candidature
2MASS0814−4020	08 14 35.46	−40 20 49.26	14.356 ± 0.023	HY
2MASS1146−4754	11 46 51.04	−47 54 38.17	14.897 ± 0.042	SI
2MASS1236−6536	12 36 32.38	−65 36 35.6	15.277 ± 0.057	PL, CA, IC, SI
2MASS1326−5022	13 26 53.48	−50 22 27.04	14.715 ± 0.037	IC, CA
2MASS1433−5148	14 33 41.95	−51 48 03.70	14.206 ± 0.034	CA, PL, SI, IC
2MASS1557−4350	15 57 27.39	−43 50 21.47	14.224 ± 0.028	PL, CA, IC
2MASS1618−3214	16 18 08.92	−32 14 36.17	14.920 ± 0.040	IC, CA, SI
2MASS1734−1151	17 34 30.53	−11 51 38.83	13.110 ± 0.028	PL
2MASS1736−0407	17 36 56.09	− 4 07 25.84	15.516 ± 0.070	SI, CA
2MASS1745−1640	17 45 34.66	−16 40 53.81	13.646 ± 0.026	SI, CA, HY
2MASS1756−4518	17 56 29.63	−45 18 22.47	12.386 ± 0.019	CA
2MASS1909−1937	19 09 08.21	−19 37 47.96	14.520 ± 0.026	CA

Table 3. Details of observing runs.

Number	Date	Telescope	Instrument	Spect. range (Å)	Dispersion (Å)
1	28/03–21/06/08	ESO-VLT-U2	UVES[1]	6700–10425[2]	0.027–0.041
2	01-09-2009–09/01/2010	ESO-VLT-U2	UVES[1]	5700–7530 & 7650-9470	0.027–0.041
3	03–05/05/2010	6.5 m Baade-Maguellan	IMACS Short-Camera[3]	6550–10000	1.98
4	15–16/02/2011	6.5 m Baade-Maguellan	IMACS Short-Camera[3]	4300–10800	1.97

[1]UVES: Ultraviolet and Visual Echelle Spectrograph.

[2]Effective range.

[3]IMACS: The Inamori Magellan Areal Camera and Spectrograph.

of 12 objects (sample B; Table 2). The data were obtained during four observing runs detailed in Table 3.

Both sets of high- and low-resolution spectra were extracted using the standard reduction procedures in the IRAF[1] TWODSPEC and ECHELLE packages, respectively: bias subtraction, flat-field division, extraction of the spectra, telluric correction as well as wavelength and flux calibration. We obtained the solution for the wavelength calibration by taking spectra of a Th-Ar lamp. The average signal-to-noise ratio (S/N) of the data, measured as the square root of the signal at ≈ 8100 Å, is ≈ 30 for UVES data (except for 2MASS2039−1126 that has S/N of ≈ 15) and ≈ 200 for both runs of IMACS data.

Fig. 1 shows high-resolution spectra of sample A on the left and low resolution spectra of sample B on the right, ordered by spectral type classification. Well-studied late-type objects with known spectral type were observed at the same time as the targets to be used as reference (M9 LP944-20; M4 GL876; and M6 GL 406) and are also included in the figure for comparison.

4 ATMOSPHERIC MODELS AND SYNTHETIC SPECTRA

To determine spectral characteristics of the targets ($T_{\rm eff}$, $\log g$, etc.), to aid us in age determination, we compared a grid of generated synthetic spectra with the observations.

According to current concepts, dust plays an important role in the formation of late M dwarf spectra (Hauschildt & Allard 1992; Tsuji, Ohnaka & Aoki 1996). Although there is no unified opinion about temperature range where dust should be considered, the temperatures of transition between dust-free and dusty models range from $T_{\rm eff} < 2600$ (Allard, Homeier & Freytag 2011) to $T_{\rm eff} < 3000$ K (Jones & Tsuji 1997).

Therefore, synthetic spectra were computed for dust-free NEXTGEN atmospheric models and for semi-empirical models (i.e. modified NEXTGEN models) in the wavelength range 6500–9000 Å. The 'dust effects' are included in semi-empirical models for M3–M8 stars. Synthetic spectra based on DUSTY, COND and corresponding semi-empirical models were calculated for M7-L0 stars.

4.1 Synthetic spectra based on NEXTGEN models

Synthetic spectra were computed for NEXTGEN atmospheric models (Hauschildt & Allard 1992) by the WITA6 program (Pavlenko 1997; Pavlenko et al. 2007). The calculations were made under the assumption of local thermodynamic equilibrium (LTE), hydro-static equilibrium, in the absence of sources and sinks of energy, for a one-dimensional model atmosphere. We used the atomic line list

from the VALD database (Kupka et al. 1999) and the line list of titanium oxide (TiO) from Plez (1998) to produce the synthetic spectra. Vanadium oxide (VO) band opacities were computed in the framework of the JOLA approximation (see Lyubchik & Pavlenko 2000). Synthetic spectra were calculated for a grid of models having $T_{\rm eff} = 2600$–3400 K with 100 K step, surface gravities of $\log g = 4.0$–5.5 with 0.5 step and metallicities of $[M/H] = 0.0$, -0.5 and -1.0 dex. Solar abundances were taken from Anders & Grevesse (1989). The artificial rotational-broadening of spectral lines was implemented following the methodology of Gray (2005) using the rotational velocity of the objects obtained in Paper II. We carried out a few numerical experiments to investigate the effect of microturbulence velocity on the spectra. The study shows that the differences in synthetic spectra associated with v_t in the 1.0–5.0 km s^{-1} range are negligible. Thus all theoretical spectra were computed for a microturbulence velocity $v_t = 3.0$ km s^{-1}.

4.2 Semi-empirical atmospheric models

We used the semi-empirical atmospheric models described in Pavlenko et al. (2007) to include the effects of dust formation. The semi-empirical models were obtained by modifying NEXTGEN, DUSTY and COND models.

The dust opacity originates in the shell-like structures lying above the photosphere (Pavlenko et al. 2007) and we expect the influence of dust in a spectrum to be more prevalent in the shortest wavelength spectral region. We assumed that dust clouds are located in the upper most layers of stellar atmosphere and do not affect the distribution of temperatures and pressures. Dusty effects were treated in two ways: (1) decreasing molecular abundance in the gas due to molecular condensation of dust particles and (2) radiation scattering in the dust clouds. The decrease in the concentration of TiO and VO molecules was modelled by two parameters: (1) the number of layers in the above model for which there is no absorption of TiO (i.e. all TiO condenses on dust particles) and (2) the coefficient of TiO molecular density reduction for all other model layers. Radiation scattering in the dust clouds was also modelled by two parameters: (1) the optical thickness of the dust cloud and 2) the location of maximum opacity as a result of these clouds. This method is described in Pavlenko et al. (2007) and Kuznetsov, Pavlenko & Gálvez-Ortiz (2012).

The theoretical spectra were computed using a semi-empirical atmospheric model for a grid with effective temperatures of $T_{\rm eff} = 2600$–3000 K (based on NEXGEN models) and $T_{\rm eff} = 2000$–2600 K (based on DUSTY and COND models) with a step of 100 K, surface gravities of $\log g = 4.0$–5.5 with a step of 0.5, and solar (Anders & Grevesse 1989) metallicity. These models were calculated for the same rotational and microturbulence velocity as for the NEXTGEN models. We are thus able to compare the observed
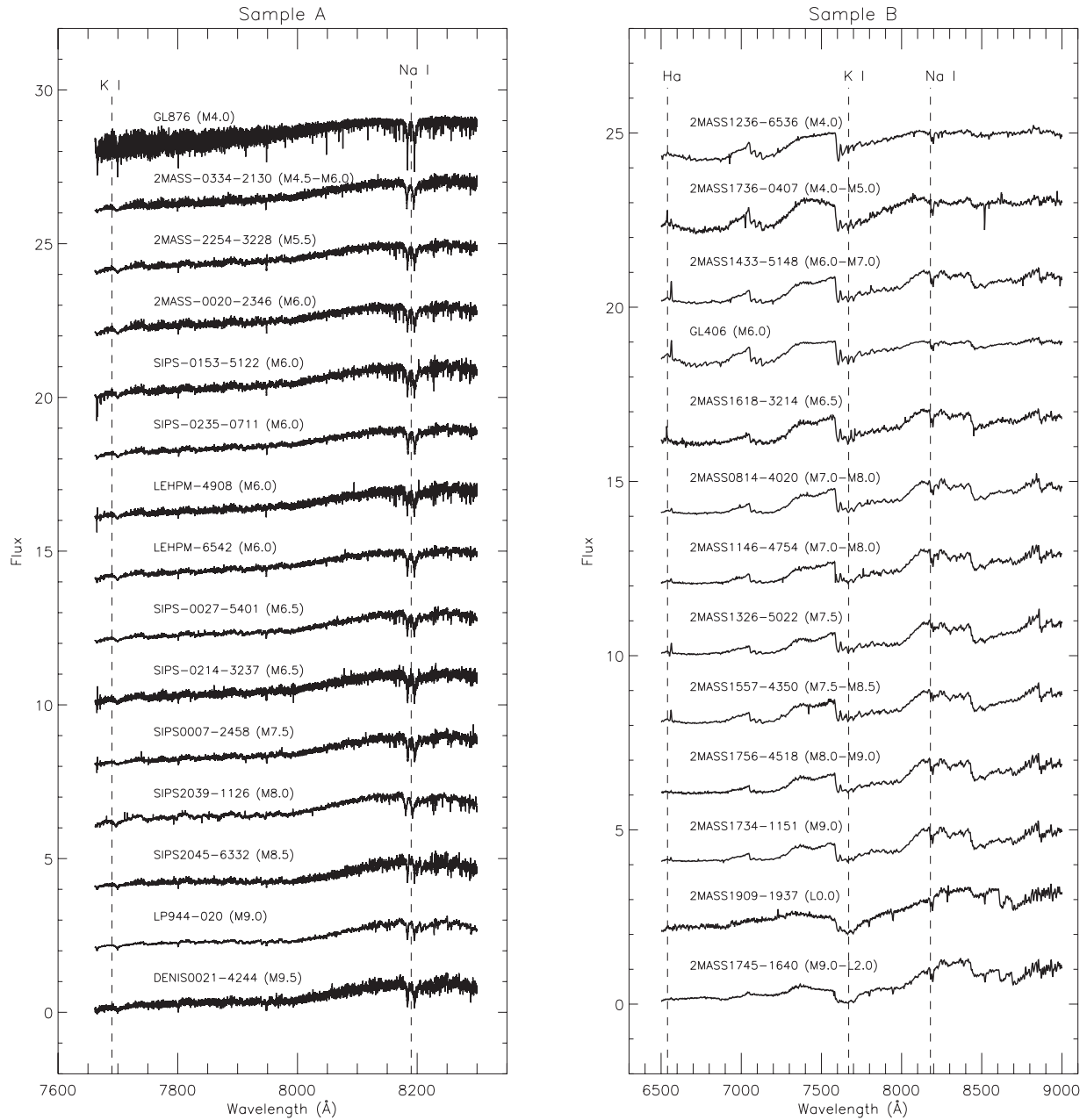
---

[1] IRAF is distributed by the National Optical Observatory, which is operated by the Association of Universities for Research in Astronomy, Inc., under contract with the National Science Foundation.

Figure 1. Left: observed SEDs of objects from sample A, the 13 targets plus reference objects in the 7600 to 8400Å range. Right: observed SEDs of objects from sample B, the 12 targets plus one reference object in the 6500 to 9000Å range. They are ordered by spectral type derived from spectroscopy.

high- and low-resolution spectra with synthetic spectra assuming both the presence and the absence of dust.

4.3 Selection of best-fitting parameters: objects with M4-M8 spectral type

The *S*-function analysis described in Pavlenko et al. (2007) was used to determine the best fit for each grid of the model independently,

$$S = \sum (f_h * H_{\mathrm{synt}} - H_{\mathrm{obs}})^2,$$

where f_h is a normalization parameter, H_{synt} is the synthetic flux and H_{obs} is the observed flux. The minimum value of *S*-function corresponds to the best fit.

The *S*-function is integrated in the 6900–7200Å, 8100–8400Å and 7660.8–7734Å, 8160–8220Å wavelength ranges for low- and high-resolution spectra, respectively. The use of these regions allowed us to analyse the TiO band at ∼7100Å and Na I (8183Å, 8199Å) doublet in low-resolution spectra, the K I (7665 and 7669Å) resonance doublet and Na I (8183Å, 8199Å) subordinate doublet in high-resolution spectra. The analysis of Na I and K I lines is significant because their profile is sensitive to T_{eff} and $\log g$. The VO (∼7400Å, ∼7800Å) bands were excluded from the fitting procedure since we do not have a satisfactory line list for this molecule.

We carried out fits of the observed spectra for two model grids, original NEXTGEN and semi-empirical, for M4-M8 objects. Figs 2 and 3 show example fits for the red part of the spectra in sample A, and the complete spectra in sample B. Figs 4 and 5 show
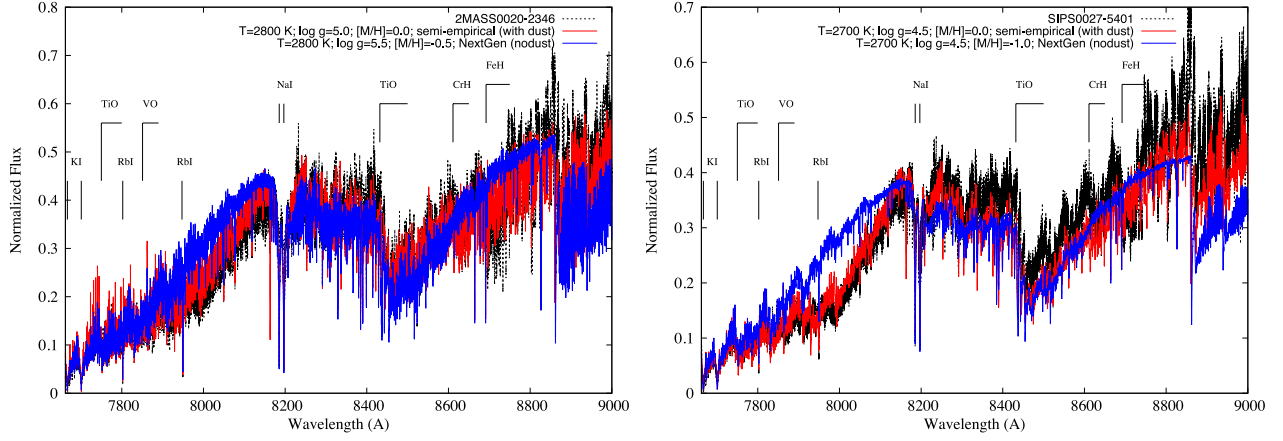
Figure 2. Sample A: random example of fits of theoretical spectra to the observed SEDs.
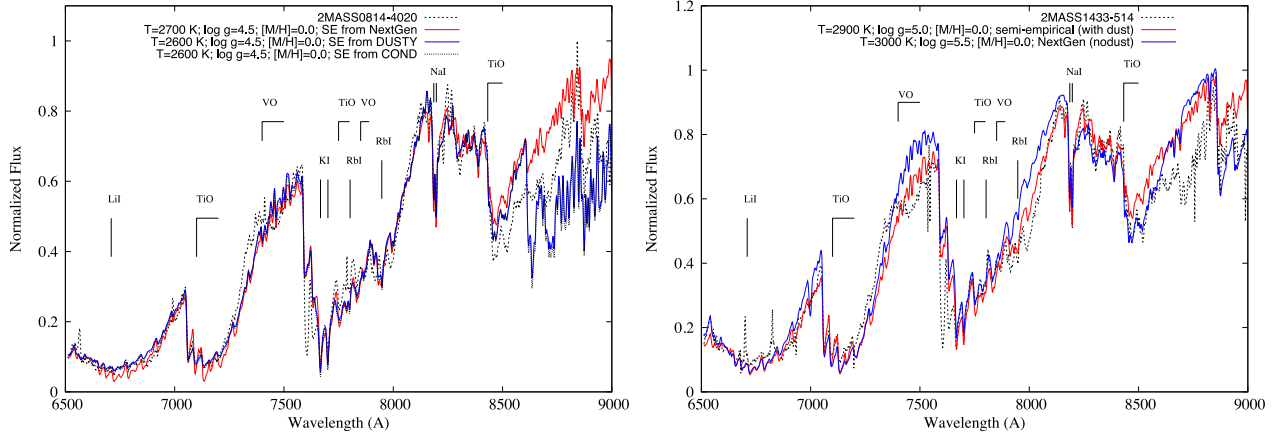

Figure 3. Sample B: random example of the best fits to the observed SEDs.
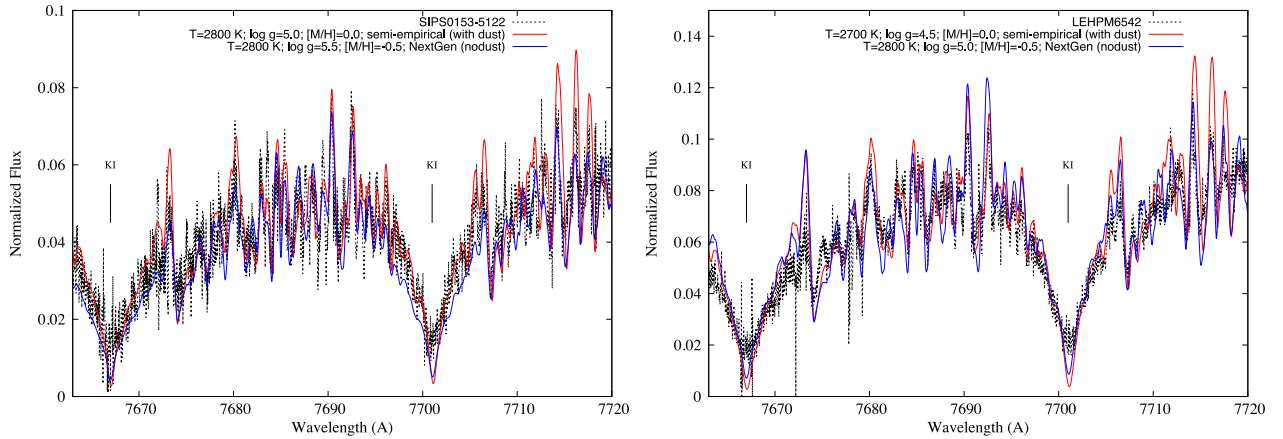

Figure 4. Sample A: random example of the best fits to the spectral regions across K I lines.

examples of the fitting of the atmospheric models, magnified around the Na I∼8190Å and K I∼7700Å doublet area for sample A. The minimum value of *S*-function for each target with M4-M8 spectral type is shown in Tables 4–7.

4.4 Analysis of objects of M8.5-M9.5 spectral type

The atmospheric structure of objects of M8.5-M9.5 spectral type differs greatly from early M dwarfs. The dust has a significant

impact on the distribution of temperature versus pressure in these atmospheres. Thus, it is incorrect to use the NEXTGEN model for objects with temperatures $T_{\rm eff} \leq 2500$ K. We used the DUSTY and COND (Allard et al. 2001) atmospheric models for the study of the late M dwarfs' synthetic spectra. The DUSTY and COND models were modified in an identical way to the model improvements for early M dwarfs: we introduced additional scattering of radiation by dust clouds and reduced the abundance of the molecules TiO and VO.
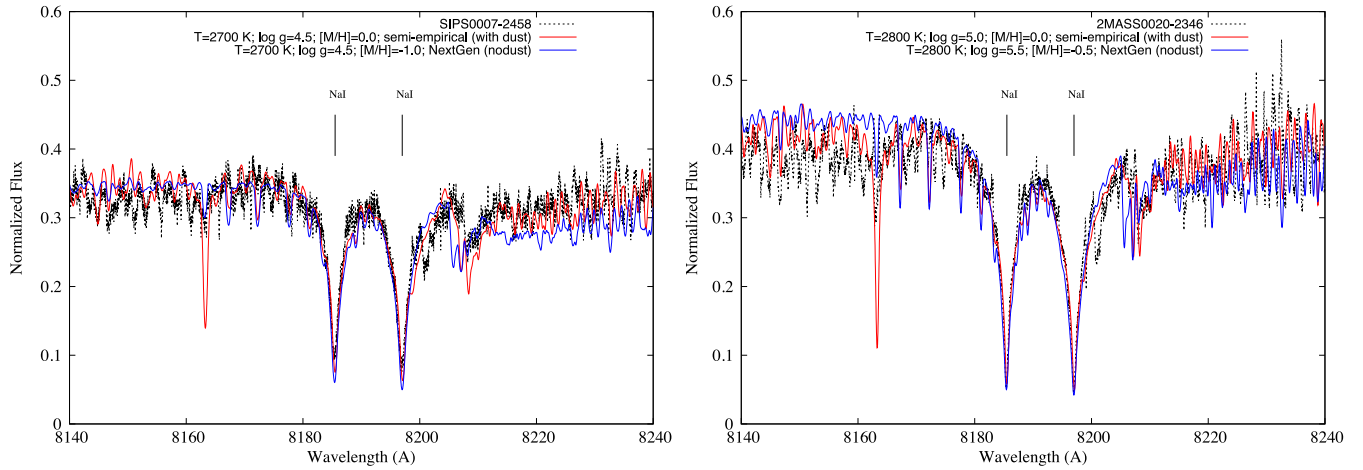
Figure 5. Sample A: random example of the best fits to the spectral regions across Na I lines.

Table 4. Sample A: model fit results for M3-M7.5 objects. Spectroscopic spectral types are from Paper II. The equivalent effective temperatures for the spectral types were taken from Reylé et al. (2011). $\Delta T_{\rm eff} = 100$ K, $\Delta \log g = 0.5$ cm s^{-2}.

Object	SpT $SpT_{\rm Spec}$	$T_{\rm eff}SpT$ (K)	$T_{\rm eff}$ (K)	NEXTGEN $\log g$ (cm s^{-2})	[M/H] dex	$S_{\rm min}$	$T_{\rm eff}$ (K)	Semi-empirical model $\log g$ cm s^{-2}	[M/H] dex	$S_{\rm min}$	Best fit[1]
GL876	M4.0	3100	3400	5.5	0.0	2.9	–	–	–	–	NEXTGEN
SIPS0007−2458	M7.5	2550	2700	4.5	−1.0	7.0	2700	4.5	0.0	6.2	s.-e.
2MASS0020−2346	M6.0	2800	2800	5.5	−0.5	4.8	2800	5.0	0.0	4.56	s.-e.
SIPS0027−5401	M6.5	2650	2700	4.5	−1.0	3.35	2700	4.5	0.0	2.70	s.-e.
SIPS0153−5122	M6.0	2800	2800	5.5	−0.5	2.42	2800	5.0	0.0	2.31	s.-e.
SIPS0214−3237	M6.5	2650	2800	5.0	−1.0	1.44	2800	5.0	0.0	1.2	s.-e.
SIPS0235−0711	M6.0	2800	2700	5.0	−1.0	0.97	2700	4.5	0.0	0.91	s.-e.
2MAS0334−2130	M4.5-M6.0	3000–2800	2800	5.5	−0.5	4.65	2800	5.0	0.0	5.65	[a]
LEHPM4908	M6.0	2800	2800	4.5	−1.0	7.02	2900	5.0	0.0	5.70	s.-e.
2MASS2254−3228	M5.5	2850	2700	5.0	−1.0	1.37	2700	4.5	0.0	1.25	s.-e.
LEHPM6542	M6.0	2800	2800	5.0	−0.5	13.5	2700	4.5	0.0	4.03	s.-e.

[1] NEXTGEN or semi-empirical (s.-e.) models.
[a] Both models are equally likely.

Table 5. Sample B: Model fit results for M3-M7.5 objects. The equivalent effective temperature for the spectral types were taken from Reylé et al. (2011). $\Delta T_{\rm eff} = 100$ K, $\Delta \log g = 0.5$ cm s^{-2}.

Object	SpT $SpT_{\rm Phot}$	$SpT_{\rm Spec}$	$T_{\rm eff}Sp$ (K)	$T_{\rm eff}$ (K)	NEXTGEN $\log g$ (cm s^{-2})	[M/H] (dex)	$S_{\rm min}$	$T_{\rm eff}$ (K)	Semi-empirical model $\log g$ (cm s^{-2})	[M/H] (dex)	$S_{\rm min}$	Best fit
2MASS1146−4754	M8.5	M7-8	∼2500	2800	5.5	−0.5	0.39	2700	4.5	0.0	0.18	s.-e.
2MASS1236−6536	M7.5	M4.0	3100	3200	5.5	0.0	0.64	2900	4.0	0.0	1.14	NEXTGEN
2MASS1326−5022	M9.0	M7.5	2550	2800	5.0	0.0	0.57	2700	4.0	0.0	0.22	s.-e.
2MASS1433−5148	M9.0	M6-7	∼2650	3000	5.5	0.0	0.58	2900	5.0	0.0	0.27	s.-e.
2MASS1618−3214	M7.0	M6.5	2650	2800	5.5	−0.5	0.69	2700	4.5	0.0	0.41	s.-e.
2MASS1736−0407	M8.5	M4-5	∼3000	3200	5.0	0.0	0.49	2900	4.0	0.0	0.55	NEXTGEN

Table 6. Sample A: Model fit results for ∼M8 object. First line refers to fit results when use NEXTGEN, DUSTY and COND models while second line refers to fit results when use the semi-empirical models based on NEXTGEN, DUSTY and COND models, respectively. Spectroscopic spectral types are from Paper II. $\Delta T_{\rm eff} = 100$ K, $\Delta \log g = 0.5$ cm s^{-2}.

Object	SpT $SpT_{\rm Spec}$	$T_{\rm eff}SpT$ (K)	$T_{\rm eff}$ (K)	NEXTGEN $\log g$ (cm s^{-2})	$S_{\rm min}$	$T_{\rm eff}$ (K)	DUSTY $\log g$ cm s^{-2}	$S_{\rm min}$	$T_{\rm eff}$ (K)	COND $\log g$ cm s^{-2}	$S_{\rm min}$	Best fit
SIPS2039−1126	M8.0	2500	2800	5.5	22.45	2600	5.0	39.96	2600	4.5	40.12	
Semi-empirical			2700	4.5	22.90	2600	4.5	20.00	2600	4.5	20.01	s.-e. DUSTY

Table 7. Sample B: Model fit results for ~M8 objects. First line refers to fit results when using NEXTGEN, DUSTY and COND models while second line refers to fit results when using the semi-empirical models based on NEXTGEN, DUSTY and COND models, respectively. $\Delta T_{eff} = 100$ K, $\Delta \log g = 0.5$ cm s^{-2}.

		SpT	NEXTGEN			DUSTY			COND			
Object	SpT_{Phot}	SpT_{Spec}	T_{eff} (K)	$\log g$ (cm s^{-2})	S_{min}	T_{eff} (K)	$\log g$ (cm s^{-2})	S_{min}	T_{eff} (K)	$\log g$ cm s^{-2}	S_{min}	Best fit
2MASS0814−4020	L4.0	M7-8	2700	5.0	0.74	2600	5.5	1.15	2600	5.0	1.22	
Semi-empirical			2700	4.5	0.35	2600	4.5	0.28	2600	4.5	0.28	s.-e. DUSTY [1,2]
2MASS1557−4350	L0.0	M7.5-8.5	2800	4.5	0.74	2600	5.5	0.93	2400	5.5	1.11	
Semi-empirical			2800	4.0	0.31	2500	4.0	0.29	2600	4.0	0.29	s.-e. DUSTY [1]
2MASS1756−4518	M7.5	M8-9	2600	5.5	0.21	2600	5.5	0.18	2600	5.0	0.20	
Semi-empirical			2600	4.0	0.09	2600	5.5	0.08	2600	5.0	0.10	s.-e. DUSTY

[1] DUSTY and COND have the same S_{min}, but DUSTY model is more appropriate in the temperature range.
[2] We could appreciate parts of the spectrum were NEXTGEN was the best fit.

Table 8. Sample A: Model fit results for M8.5-M9.5 objects. First line refers to fit results when using DUSTY and COND models while second line refers to fit results when using the semi-empirical models based on DUSTY and COND models, respectively. Spectroscopic spectral types are from Paper II. The equivalent effective temperature for the spectral types was taken from Dahn et al. (2002). $\Delta T_{eff} = 100$ K, $\Delta \log g = 0.5$ cm s^{-2}.

	SpT		DUSTY				COND				
Object	SpT_{Spec}	$T_{eff}SpT$ (K)	T_{eff} (K)	$\log g$ (cm s^{-2})	[M/H] (dex)	S_{min}	T_{eff} (K)	$\log g$ (cm s^{-2})	[M/H] (dex)	S_{min}	Best fit
DENIS0021−4244	M9.5	2300–2400	2000	5.5	0.0	7.85	2400	5.5	0.0	13.40	
Semi-empirical			2400	4.0	0.0	5.89	2500	4.0	0.0	6.62	s.-e. DUSTY
SIPS2045−6332	M8.5	2300–2400	2000	5.5	0.0	11.39	2400	4.0	0.0	17.19	
Semi-empirical			2400	4.0	0.0	8.14	2500	4.0	0.0	10.30	s.-e. DUSTY
LP944-20	M9.0	2300–2400	2000	5.5	0.0	0.42	2400	5.5	0.0	0.57	
Semi-empirical			2400	4.0	0.0	0.29	2400	4.0	0.0	0.35	s.-e. DUSTY

Table 9. Sample B: Model fit results for >M8.5 objects. First line refers to fit results when using DUSTY and COND models while second line refers to fit results when using the semi-empirical models based on DUSTY and COND models, respectively. The equivalent effective temperature for the spectral types were taken from Reylé et al. (2011). $\Delta T_{eff} = 100$ K, $\Delta \log g = 0.5$ cm s^{-2}.

		SpT		DUSTY				COND				
Object	SpT_{Phot}	SpT_{Spec}	$T_{eff}SpT$ (K)	T_{eff} (K)	$\log g$ (cm s^{-2})	[M/H] (dex)	S_{min}	T_{eff} (K)	$\log g$ (cm s^{-2})	[M/H] (dex)	S_{min}	best fit
2MASS1734−1151	L0.0	M9.0	2300–2500	2600	5.5	0.0	1.34	2600	5.0	0.0	1.43	
Semi-empirical				2400	4.0	0.0	0.79	2400	4.0	0.0	0.86	s.-e. DUSTY
2MASS1745−1640	L8.0	M9-L2	~2300–2000	2000	5.5	0.0	0.06	2200	5.5	0.0	0.07	
Semi-empirical				2000	5.5	0.0	0.05	2200	5.5	0.0	0.05	s.-e. DUSTY
2MASS1909−1937	M9.0	L0.0	~2200	2100	3.5	0.0	0.55	–	–	–	–	
Semi-empirical				2000/2100	6.0/3.5	0.0	0.45	–	–	–	–	s.-e. DUSTY ?

As with earlier spectral types, we utilized fits to the TiO and VO absorption bands and the K I and Na I doublets, to determine the stellar fundamental parameters. In weakly ionized atmospheres at $T_{eff} < 3000$ K the natural broadening is several orders of magnitude weaker than pressure and Stark broadening, and can thus be neglected. The broadening of K I and Na I resonance lines is dominated by pressure effects, but the theory of this is not particularly advanced. Pressure broadening is calculated using two methods: a collisional approximation (van der Waals theory) and quasi-static theory (see Allard et al. 2003; Burrows & Volobuyev 2003). The use of a collision approximation allows us to describe the profiles of metal lines in early M dwarfs. The quasi-static theory is used in the study of L dwarfs, where energy levels of atomic sodium or potassium are immersed in a sea of molecular hydrogen and are subsequently perturbed by the potential field of the diatomic hydrogen. The modelling of atomic-line broadening for objects that are close to the transition between M and L spectral classes is complicated and this issue is beyond the scope of this paper. Since in our case we could see only the core of the lines and do not see

extended wings, our fits should be sufficient without including any broadening.

Physical properties were derived for objects with M8.5-M9.5 spectral types based on the fitting of high- or low-resolution spectra and synthetic spectra calculated for COND and DUSTY models. In addition, *S*-function analysis provided the best fits. Since in sample B there are some objects classified as M8, we applied fits with the synthetic spectra (NEXTGEN, DUSTY and COND) as well as with appropriate semi-empirical models, to provide the transition between the NEXTGEN and the DUSTY/COND models. Results of these fits are shown in Tables 6–9.

LP944-20: LP944-20 is a known BD of spectral type M9 and we used it as a test for the atmospheric fits as well as to benchmark the age constraints described in following sections. Several authors have studied this object in detail to determine its characteristics. Tinney (1998) estimated an age between 475 and 650 Myr by evolutionary tracks, while Ribas (2003) determined LP944-20 as a kinematic member of the Castor MG and therefore estimated an age of 320 ± 80 Myr. Pavlenko et al. (2007) used

semi-empirical atmospheric models to determine the parameters of LP944-20 including lithium abundance, of which the best fit gave log N(Li) = 3.25 ± 0.25, and found a similar age to the one found by Ribas (2003).

According to previous studies the effective temperature of LP944-20 is in the range $2040 \le T_{eff} \le 2400$ K (see Basri 2000; Dahn et al. 2002; Pavlenko et al. 2007). The best fit obtained here, with the DUSTY model, provides $T_{eff} = 2400$ K and log $g = 4.0$ (see Table 8). The log g obtained by Pavlenko et al. (2007) was 4.5, with temperatures of 2000–2200 K using COND models. They remarked that temperatures in the outermost layers of the DUSTY models were higher in comparison to the COND models. This difference is consistent within the uncertainties.

4.5 Results

All the targets in sample A, with the exception of 2MAS0334−2130, present a better fit when a semi-empirical model with dust is used instead of the dust-free NEXTGEN model, as shown by S_{min} of Table 4. This would imply that the presence of dust should be taken into account for effective temperatures up to ≈2900 (Jones & Tsuji 1997; Kuznetsov et al. 2012).

Similarly to LP944-20, the two targets of sample A cooler than M8 spectral type are better fitted by the DUSTY model (Tables 6 and 8, and Figs 2, 4 and 5).

For the analysis, we divided sample B into three different spectral type ranges for the fits: <M8, >M8 and as we have many objects with an M8 spectral classification we treated them as a third set and applied both sets of models for them (see Section 4.4).

We used GL 406 (M6.0) as reference star to test spectral typing and model fits. However, we noticed that the flux calibration is very poor for $\lambda < 7500$Å. The cause is uncertain since all other spectra were calibrated correctly. The K I and Na I lines were not present in the fault area, hence we centred our fit on $\lambda > 7500$Å.

Results of objects that were spectroscopically classified as earlier than M8 are shown in Table 5, where S_{min} is given in Columns 8 and 12. From these targets, four present a better fit with a semi-empirical model with dust, and two, 2MASS1236−6536 and 2MASS1736−0407, with NEXTGEN. These two were included in our sample due to their 'cold photometric' classification (Section 3.2) but spectral classification and model fit suggest warmer temperatures.

For objects classified as M8, we applied all models. Results are given in Table 7. In the case of 2MASS0814−4020, DUSTY and COND models have the same S_{min}, but the DUSTY model is more appropriate for the target's temperature. Also, despite the higher value of S_{min} for the NEXTGEN model, we could appreciate by visual inspection and by the S-function value that in parts of the spectrum NEXTGEN was the best fit. For 2MASS1557−4350, the DUSTY and COND models also have the same S_{min}. We chose the DUSTY model as being more appropriate for its temperature.

For objects with spectral types later than M8, parameters determined from the best fit to the observed SEDs are given in Table 9. In this case, it was not easy to find a good fit for the blue part of the spectrum ($\lambda < 7500$Å). In the case of 2MASS1909−1937 no COND model provided an acceptable result and the DUSTY model gave no reliable gravity values. It is likely that these objects are also suffering from relatively uncertain flux calibration, but the fact that these are the coolest objects and around the M-L transition may indicate other issues like the use of an inappropriate set of models. Since the K I and Na I spectral regions seem to be correctly fitted we keep the results but consider them with caution for 2MASS1734−1151

and 2MASS1745−1640, while we could not extract any acceptable conclusion from the fit for 2MASS1909−1937 (see Table 9).

5 AGE CHARACTERISTIC

Sample A is formed of objects that are already confirmed as kinematic candidates of MGs. Since kinematics is not sufficient to confirm membership, determination of a candidate's age can further constrain its group membership to a point of robustness or dismiss it as an old field target that shares kinematics with a young MG. For our candidates, age in some cases can also discriminate between multiple MG candidatures. Sample B is formed of astrometric candidates and so further study should be applied to confirm any membership. This can be achieved by: (1) using gravity sensitive spectroscopic features to distinguish between young and old ultracool dwarfs, (2) using the activity/age relation for late-type stars up to a spectral type of M7 (Mochnacki et al. 2002; Silvestri et al. 2006; Reiners & Basri 2008; Jenkins et al. 2009), (3) measuring the lithium 6708Å doublet (e.g. Rebolo et al. 1996; Pavlenko et al. 2007) as the abundance of lithium is related to mass and age for substellar objects and (4) determining $v \sin i$ to differentiate between young and older M types.

Fig. 9 of Paper I shows a plot of evolution-time (based upon potential group membership) versus spectral type for the complete sample of candidates. The figure, reproduced and updated here as Fig. 6, illustrates how an object would be selected for various
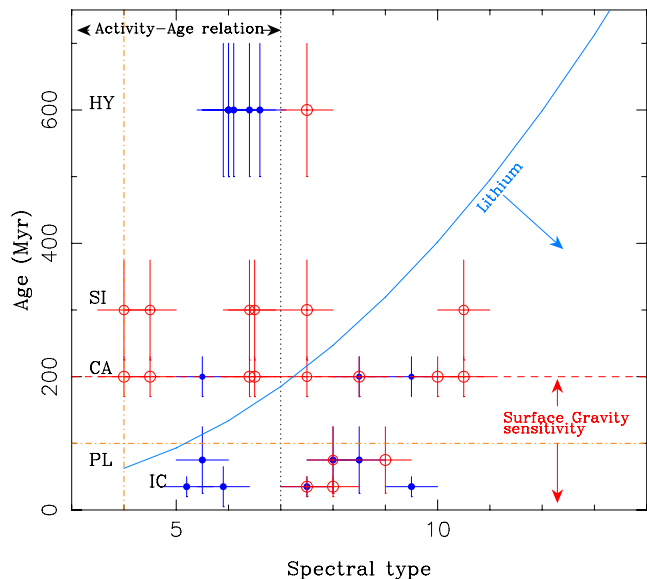

Figure 6. This figure (updated fig. 9 from Paper I) illustrates how an object would be selected for the various methods of age constraining. Candidates that appear to the right of the lithium edge (blue continuous line) can be followed up with a lithium test programme. Objects that appear younger than 200 Myr (horizontal red dashed line) are eligible for follow-up using spectroscopic gravity-sensitive features. Vertical and horizontal orange dot–dashed line represents the Schlieder et al. (2012) limits for the Na I diagnostic applicability. We here took into account the 200 Myr limit. Candidates that fall to the left of the spectral type = M7 limit (vertical black dotted line) would thus be suitable for age/activity relation follow-up, although candidates with a spectral type close to M7 may be subject to large uncertainties on their age. Some candidates cannot be tested by any of these methods but will be eligible for age testing using $v \sin i$. Sample A targets are plotted as blue filled circles and sample B as red open circles. We plotted up to two candidatures for targets with multiple MG.

methods of age constraining follow-up mentioned. Candidates that appear to the right of the lithium edge can be followed up with a lithium test programme. Objects that appear younger than 200 Myr are eligible for follow-up using spectroscopic gravity sensitive features. Candidates that fall to the left of the spectral type M7 would thus be suitable for age/activity relation follow-up, although candidates with a spectral type close to M7 may be subject to large uncertainties on their age. Some candidates cannot be tested by any of these methods but will be eligible for age testing using $v \sin i$.

In Paper II we presented a $v \sin i$ study (for sample A) where we applied this criterion of youth based on figs 9 and 10 of Reiners & Basri (2008) to support group membership (see Paper II). We study here the rest of the age-constraining features.

5.1 Surface gravity features

The radius of young UCDs can be as much as three times greater than their eventual equilibrium state (Burrows et al. 2001), and as a result young objects can exhibit significantly lower surface gravities (10–100 times) than their evolved counterparts with the same spectral type. Low-resolution (e.g. $R\sim$350–2000) studies in the optical (Martín, Rebolo & Zapatero Osorio 1996; Luhman, Liebert & Rieke 1997; Martín et al. 2010) and infrared (Jones et al. 1996: Gorlova et al. 2003; McGovern et al. 2004) have demonstrated that numerous features (e.g. CaH, K I, Na I, VO, etc.) can be used as gravity-sensitive (and thus age-sensitive) diagnostics for young objects. Diagnostics should be sensitive to gravity and age for objects that are younger than $\sim$200 Myr (e.g. Barrado y Navascués 2006). Schlieder et al. (2012) presented a study of the Na I doublet equivalent width in giants, old dwarfs, young dwarfs, and candidate members of the β Pic MG using medium-resolution spectra. They concluded that the diagnostic is reliable for objects with spectral types later than M4 and younger than 100 Myr, and that metallicity has an important role. Therefore, this youth indicator is best used on samples with similar metallicity. Thus, we aimed to apply this test by determining the surface gravity of the younger MG candidates, although we took into account all candidates up to 200 Myr.

As mentioned before, the main atomic gravity-sensitive features present in our spectra are: the K I resonance doublet (7665 and 7669Å) and the Na I subordinate doublet (8183 and 8199Å). We fitted the spectra of the candidates with a synthetic model (see Section 4) to determine the log g of both samples A and B (Table 4–9). Figs 4 and 5 show some examples of atmospheric model fitting magnified on the aforementioned features for sample A.

We performed two approaches in the surface gravity studies: inferring age-limits from (1) the surface gravity obtained from the best fit synthetic models and (2) comparison of the equivalent width of gravity-sensitive Na I doublet.

5.1.1 *Values of log g from synthetic model fits*

As mentioned above, surface gravity features can be studied to discriminate if an object is young or old, but it is not easy to associate a log g value to an age interval, that is, to have an absolute log g–age relation. Many parameters affect the derived log g: atmospheric model used, resolution and instrument. Therefore we observed LP944-20, with known age and previously fitted by different models, to set the range of log g–age interval for our observations and as a test object for our method of late M dwarf investigation.

Taking into account the association with the Castor MG and the age based on the presence of lithium, we used our log g for LP944-20

as a reference and compared it to the log g of the candidates. From this, we assume that an object with spectral type and log g similar to LP944-20 is probably of similar age. Models from the literature (e.g., NEXTGEN, DUSTY, COND) associate similar or lower ages with warmer objects with the same log g than to those that are cooler. For example, selecting log g in the 4.0–4.5 range in DUSTY and COND models, an object with $T_{\text{eff}} = 2400$ K intersects 8–30 Myr age isochrones, whilst objects with $T_{\text{eff}} \geq 2400$ K intersect 5–7 Myr, and objects with $T_{\text{eff}} \leq 2400$ K intersect with isochrones over 40 Myr. Both the DUSTY and COND models present ambiguities for 30 Myr isochrones. The COND model presents similar problems for $\geq$40 Myr isochrones, but fortunately in this case with temperature ranges far from that of our targets. Therefore, we can assume that objects warmer than LP944-20 would have, in general, ages $\leq$200–300 Myr should they have log $g = 4.0$.

Since LP944-20 is only a single object, in order to constraint this log g–age relation, we also used the GL 876 field target, observed with the candidate A sample. This allows us to compare our target log g values with those of old and intermediate-age targets.

We fit them in the same way as our candidates and results of the best fit are given in Tables 4 and 8.

As mentioned in Section 4.4, LP944-20 is a known member of the Castor MG (age $\sim$ 200 Myr), and Pavlenko et al. (2007) obtained an age of $\sim$300 Myr through lithium depletion. Applying the atmospheric model method described in Section 4, we obtained a log g of 4.0 ± 0.5.

GL 876 is an M4 dwarf. It is known as an exoplanet host of four planets. Literature provides a few age calculations, such as 1–10 Gyr from Marcy et al. (1998), >1 Gyr from Shanklad et al. (2006) and 0.5–1 Gyr from Correia et al. (2010). Despite the variations it is clearly an old object that should show a high value of gravity. We find that the NEXTGEN model best fit provides a log g of 5.5 ± 0.5.

To set the age–gravity relation for our sample, we used these results as a basis. Log g obtained values of the candidates are 4.0, 4.5, 5.0, and 5.5, where we can state that objects with log $g = 4$ are young and still in contraction and that objects with log $g = 5.5$ are old. With a 0.5 uncertainly, an object with log g of 4.5 (4.0–5.0) shows ambiguity when discriminating between young and old.

Accepting the limitations and the uncertainty in the constraints, spectral type and metallicity dependence, etc., for the atmospheric fits to our sample, objects with log $g \approx 4.0$ are probably young (under $\sim$200 Myr), objects with log $g \approx 4.5$ are older but possibly still in contraction ($\sim$300 Myr), and therefore objects with log $g \approx 5.0$ and log $g \approx 5.5$ are probably older than 300 Myr.

The log g obtained with model comparison are given in Columns 5 and 9 of Tables 4 and 8, Columns 6 and 10 of Tables 5 and 9, and Columns 5, 8 and 11 of Tables 6 and 7.

5.1.2 *Na I equivalent width (EW) comparison*

Additionally, we checked if *EW*(Na I) measurements can be used to determine youth, based on Martín et al. (2010) and Schlieder et al. (2012).

Given the cool nature of the targets, the measurement of equivalent widths in the optical are generally measured relative to the observed local pseudo-continuum formed by molecular absorptions (mainly TiO), and therefore the *EW*s are 'pseudo-equivalent widths' (Pavlenko 1997; Zapatero Osorio et al. 2002). However, we will call them *EW* for simplicity hereafter.

Although there is considerable scatter in the data (mainly from the use of different instruments) Martín et al. (2010), fig. 3, plot

Table 10. MG membership parameters. For each target, we give the result obtained for each criterion used. N/A = non-applicable criterion in this case; Y = the age parameter agrees with the MG membership; N = the age parameter does not agree with the MG membership; when more than one membership was possible in Column 5, the MG name that the criteria determined as possible are given. Where HY is Hyades, SI is Ursa Major, IC is IC 2391, CA is Castor and PL is Pleiades MG and YD is other young disc object. When interrogation appears after MG name we indicate that the membership probability is fewer than for other MGs or in the case of 2MASS1734−1151 and 2MASS1909−1937 that the criteria are not conclusive.

Object	$EW(\mathrm{Na\,I})^1$ (Å)	$EW(\mathrm{H}\alpha)^2$ (Å)	Age[2] (Myr)	MG memb. (Kinem/Astrom)[3]	M. from $EW(\mathrm{Na\,I})^1$	M. from $EW(\mathrm{H}\alpha)^2$	M. from $\log g^4$	M. from Li I[5]	M. from $v \sin i^6$	Final MG
SIPS0007−2458	8.2	11.0	1–300	IC	N	Y	Y	N	Y	*YD*
2MASS0020−2346	8.1	6.1	∼300	YD	Y	Y	Y	?	Y	*YD*
DENIS0021−4244	8.4	^{a}	N/A	IC, CA	CA	N/A	Y	–	N	*CA*
SIPS0027−5401	7.7	8.1	∼300	HY	N/A	Y	Y	Y	Y	*HY*
SIPS0153−5122	8.0	7.5	∼300	IC, HY	HY	HY	HY	HY	Y	*HY*
SIPS0214−3237	7.9	8.4	∼300	HY	N/A	Y	Y	Y	Y	*HY*
SIPS0235−0711	7.9	7.7	≥300	HY	N/A	Y	Y	Y	Y	*HY*
2MASS0334−2130	7.3	11.5	1–300	IC	N	Y	N	N	?	*YD*
SIPS2045−6332	6.3	2.1	N/A	PL, CA	CA	N/A	Y	Y	?	*CA*
SIPS2039−1126	7.3	–	–	PL	N	–	Y	Y	Y	*PL*
LEHPM4908	7.3	6.5	∼300	HY	N/A	Y	Y	Y	–	*HY*
2MASS2254−3228	8.5	5.8	∼300	PL, CA	CA	CA	Y	–	Y	*CA*
LEHPM6542	7.6	4.9	≥300	HY	N/A	Y	Y	Y	Y	*HY*
2MASS0814−4020	9.0	7.2	≥300	HY	N/A	Y	Y	N/A	N/A	*HY*
2MASS1146−4754	7.9	5.2	≥300	SI	N/A	Y	Y	N/A	N/A	*SI*
2MASS1236−6536	5.8	1.0	300–1200	PL, IC, CA, SI	CA, SI	CA, SI	N	N/A	N/A	*CA, SI*
2MASS1326−5022	4.2	23.6	1–100	IC, CA	IC	IC	Y	N/A	N/A	*IC*
2MASS1433−5148	7.9	19.8	1–100	PL, IC, CA, SI	CA, SI	PL, IC	SI	N/A	N/A	*CA?, SI*
2MASS1557−4350	4.0	16.4	1–100	PL, IC, CA	PL, IC	N/A	Y	N/A	N/A	*PL, IC*
2MASS1618−3214	8.0	7.8	1–300	IC, CA, SI	CA, SI	Y	Y	N/A	N/A	*IC?, CA, SI*
2MASS1734−1151	7.7	5.5	N/A	PL	N	N/A	Y	N/A	N/A	*PL?*
2MASS1736−0407	6.1^b	4.2	50–300	CA, SI	N/A	Y	Y	N/A	N/A	*CA, SI*
2MASS1745−1640	5.6	1.4	≥300	CA, SI, HY	Y	N/A	HY	N/A	N/A	*CA?, SI?, HY*
2MASS1756−4518	7.5	3.2	N/A	CA	N/A	N/A	Y	N/A	N/A	*CA*
2MASS1909−1937	6.3	^{a}	N/A	CA	N/A	N/A	–	N/A	N/A	*CA?*

[1]Equivalent width of the Na I doublet as explained in Section 5.1.
[2]See Section 5.2.
[3]MG membership from kinematic (sample A) or from photometric and astrometric criteria (sample B) (see Section 2).
[4]From values obtained in the synthetic fits, given in Columns 5 and 9 of Tables 4–6.
[5] Only applicable for high-resolution data (see Section 5.3).
[6]From Paper II.
^{a}Absorption line filled in with emission.
^{b}Measured with a cosmic ray in the line.

Na I *EW* versus spectral class for a few field objects and members or candidates of the Upper Scorpii OB association. To measure consistent equivalent widths in spectra of different resolutions, they established as a rule that the pseudo-continuum region was between 823 and 827 nm, and integrated the line from 817.5 to 821.0 nm. Their figure shows a clear trend, and they inferred that objects with the weakest Na I are likely to have low surface gravity. They established as a rule of thumb that any object with spectral class between M6 and L4 and with a Na I doublet detectable but weaker than field counterparts observed with the same spectral resolution is likely to have a low surface gravity and consequently a very young age (i.e. younger than 100 Myr) and substellar mass. Sample B have similar resolution to the Martín et al. (2010) data. As such we measured the combined equivalent widths of the two lines of the Na I doublet in the same manner (given in Table 10) allowing direct comparison. In the case of sample A, we convolved the spectra to the same resolution and then measured *EW*(Na I). The left panel of Fig. 7 presents equivalent widths of the Na I doublet versus spectral type for all targets of sample A as blue crosses, and B as red filled circles, with the Martín et al. (2010) data: 65 high-gravity field objects are plotted as six pointed asterisks, six low-gravity objects

as open triangles, 12 reference field stars as open circles and seven Upper Sco candidates as solid hexagons.

While the metallicities of all MGs are similar to solar, the Upper Sco cluster does not yet have a robust metallicity determination, and other objects in Martín et al. (2010) have different metallicities. We took the information from *EW*(Na I) studies in Schlieder et al. (2012) into account when comparing samples A and B with Martín et al. (2010).

For sample A, if we look into MG candidatures (thus age) and *EW*s(Na I), they are inconsistent (Table 10, column 2). That is to say that some young MG candidates present a higher *EW*(Na I) than others which have candidature to older MGs. But if we take into account the final MG membership given in column 11 of Table 10, most of sample A targets are finally classified as candidates to MGs with ages ≥∼200 Myr (except one, SIPS2039−1126), and therefore the *EW*(Na I) become consistent (see Fig. 7, right panel). SIPS0007−2458 and 2MASS0334−2130, both candidates to IC2391, present values of *EW*(Na I) too high for IC2391 age. Since we obtained *EW*(Na I) = 6.5 for LP944-20, the value of *EW*(Na I) = 7.3 for SIPS2039−1126 is comparatively high for its Pleiades membership. Convolution might have introduced
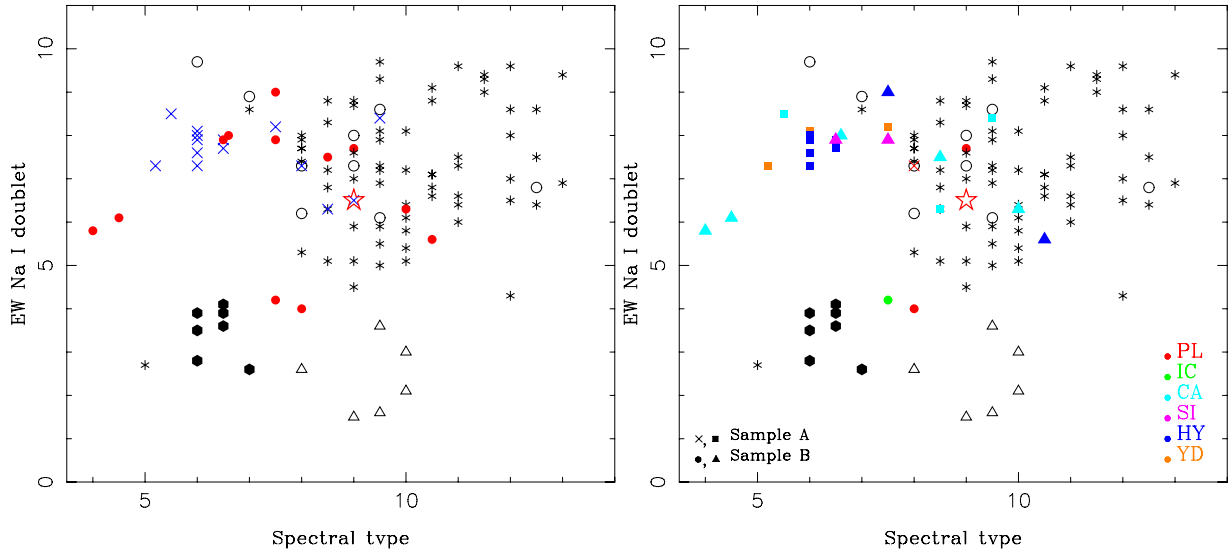
Figure 7. The right and left panels show two versions of the same information with different legends in order to highlight different information. Left: from Martín et al. (2010), 65 high-gravity field objects are plotted as six pointed asterisk symbol, six low-gravity objects as open triangles, 12 reference field stars as open circles and seven Upper Sco candidates as solid hexagons. We overplot sample A as blue crosses, and sample B as red filled circles. The red star marks LP944-20. Errors are approximately the size of plot symbols. Right: here we overplot to Martín et al. (2010) data, sample A (crosses and filled squares), and sample B (filled circles and triangles), plotted in different colours depending on their final MG membership candidature (Table 10). When objects present more than one candidature, we plotted the membership to the youngest MG. To better discriminate young targets, we use triangles and squares for candidates finally classified as possible member of MGs with ages $\geq$200 Myr while crosses and circles are candidates finally classified as possible member of MGs with ages <200 Myr (see Section 6).

additional noise affecting the comparison and we discuss further this target in Section 5.3.

For sample B, if we look into MG candidatures and *EW*s(Na I) (Table 10, Column 2), they are consistent. That is, in general, target candidates to IC2391 and the Pleiades show the lowest *EW*s, candidates to Castor and Sirius show higher, intermediate *EW* values and candidates to Hyades show the highest values of *EW* (Fig. 7, right panel). The two targets showing low values of *EW*s(Na I) are 2MASS1326−5022, candidate to IC 2391, and 2MASS1557−4350, candidate to Pleiades and IC 2391. The rest of the candidates show higher values in agreement with their MG candidatures except for 2MASS1734−1151, M9 candidate to Pleiades but showing larger values of *EW*s (Na I) than LP944-20.

5.2 Activity versus age relation

Subsequent studies by Skumanich (1972) show that activity decreases over time for late-type stars. However, after a spectral type of ≈ M3–4, stars become fully convective and the activity is driven by a turbulent dynamo in a mechanism that is still not clear. Many studies have found evidence that the age–activity relation extends into the M dwarf regime (see e.g. Mochnacki et al. 2002; Mohanty & Basri 2003; Silvestri et al. 2006; Reiners & Basri 2008). Recently, some authors (Berger et al. 2008; West et al. 2008) have shown that the fraction of active M0-M7 stars decreases with the vertical distance from the Galactic plane, further evidence of an age–activity relation. Comparing activity data to dynamical simulations, West et al. (2008) derive an 'activity lifetime' relation for M dwarfs of spectral type M0-M7 in the range 0.4–8 Gyr. Following this, we can identify older non-MG UCDs in our sample through lack of chromospheric emission.

Comparing activity levels of our sample with activity levels of objects of the same spectral type and with known age, we can infer age ranges for our targets that would help us to confirm (or

otherwise) their MG membership in the same way of other literature examples such us Stauffer, Liebert & Giampapa (1995; fig. 13), Stauffer et al. (1997; fig. 8), Terndrup et al. (2000; fig. 9), Barrado y Navascués, Stauffer & Jayawardhana (2004; fig. 5), Shkolnik, Liu & Reid (2009; fig. 13).

Although there are several chromospheric activity indicators (Ca II H&K, Balmer lines, Ca II infrared), we used the Hα emission since it is included in the spectra presented here (with the exception of the SIPS2039−1126 spectrum). Young M dwarfs generally have Hα in emission, with the average equivalent width increasing to later spectral types (e.g. West et al. 2004). Generally, the level of chromospheric activity is measured by comparison of the diagnostic line's flux, but for M dwarfs equivalent width is also used. We derived Hα pseudo-equivalent widths by direct integration of the line profile using the SPLOT task in IRAF, however, we will utilize them as *EW*s.

Taking into account that *EW*(Hα) will reflect any activity variability, often present in young objects, and that MGs with different ages will show different activity saturation levels as well as a higher dispersion in the level of activity when they are older (see e.g. Stauffer et al. 1997, Pizzolato et al. 2003; Ryan, Neukirch & Jardine 2005; López-Santiago 2005; Martínez-Arnáiz et al. 2011), we compared the *EW*(Hα) versus spectral type of our candidates with objects of known age.

We compiled a sample of M dwarfs with known age and *EW*(Hα) from the literature. These were taken from Hyades and Pleiades members in Terndrup et al. (2000), young and old disc and field stars in Mohanty & Basri (2003) and from a compilation of targets with ages determined by different methods in Shkolnik et al. (2009). When using targets with MG or cluster memberships, we assigned them the age of the cluster. From Mohanty & Basri (2003), we assigned an averaged value of 500 Myr to YD, 600 Myr to YO (old-young), 1 Gyr for OD and more than 1200 Myr for Halo targets.
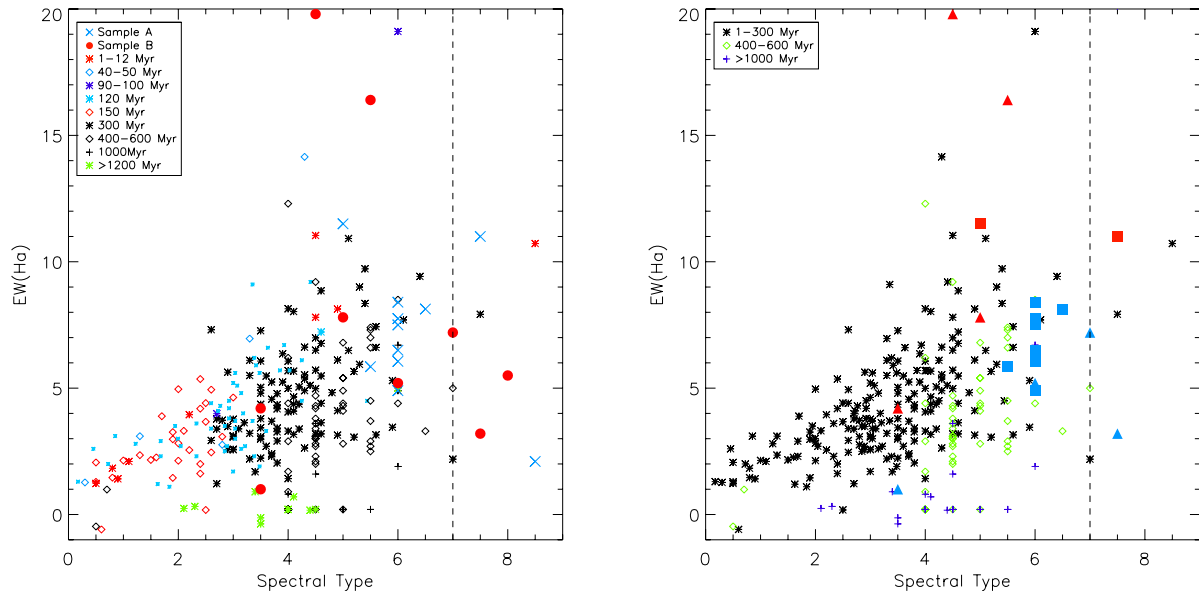
Figure 8. $EW(H\alpha)$ versus spectral type. In the same way as in Fig. 7, both panels show two versions of the same information with different legends in order to highlight different information. Left: Sample A is plotted as blue crosses, Sample B as red circles and literature known-age objects in different symbols according to age: red asterisk for objects with age between 1 and 12 Myr, blue diamonds for 40 and 50 Myr, violet asterisk for 90 and 100 Myr, blue asterisk for 120 Myr, red diamonds for 150 Myr, black asterisk for 300 Myr, black diamonds for 400 Myr and green asterisk for objects with ages over 1200 Myr. Literature data have been obtained from Terndrup et al. (2000), Mohanty & Basri (2003) and Shkolnik et al. (2009) where ages were calculated by known-age MG or Cluster membership or by other age constraining methods. Right: similar to left panel where to favour the age discrimination we plot only three age intervals. Sample A targets are plotted as filled squares and sample B as filled triangles, where targets classified with ages ≥300 Myr are plotted in blue and targets with ages <300 Myr are plotted in red.

The $EW(H\alpha)$ of our object is given in column 3 of Table 10. Fig. 8 (left-hand panel) presents $EW(H\alpha)$ versus spectral type for our candidates, with blue crosses and red filled circles for sample A and B, respectively, in comparison with data from the literature.

In the right-hand panel of Fig. 8, only three ranges of ages are plotted to better discriminate the possible age interval of our samples. Sample A targets are plotted as filled squares and sample B as filled triangles, where targets classified with ages ≥300 Myr are plotted in blue and targets with ages <300 Myr are plotted in red.

Although theoretically equal, equivalent widths measured in lower resolution spectra can be slightly larger than measured in higher resolution spectra (due to line blending), and pseudo-equivalent width measurements show variation with resolution, therefore there is a possibility that variability effects are seen in our observations. Taking into consideration that only one data point is available for each of our candidates (and therefore variability cannot be determined), that older MG members can present higher scatter, and that for sample B, values of $EW(H\alpha)$ have been measured at low resolution, we have determined a rough age interval for 18 of the candidates (we have included targets in the limiting spectral type M7 and M7.5.).

We have assumed that the candidates are single objects. Any stellar or substellar companion would probably increase the activity levels making the targets look younger when we measure $EW(H\alpha)$ (e.g. Basri et al. 1985; Rutten 1987; Schrijver & Zwaan 1991; Gálvez-Ortiz 2005).

All targets in samples A and B with spectral types under M7.5 have $EW(H\alpha)$ values inside the limits of an age that agree with at least one of their MG candidature (see Columns 3 and 4 of Table 10 and Fig. 8).

It should be noted that the SIPS2039−1126 spectrum does not include the Hα region, thus the activity criterion has not been used in this case.

5.3 Lithium

The Li I doublet at 6708Å is an important diagnostic of age in young late-type stars. Lithium is destroyed in fully convective low-mass objects, with mass from 0.3 to $0.06\,M_\odot$ (e.g. Rebolo et al. 1996) as all acquire core temperatures $>2\times10^6$ K as they heat up during early contraction. Convection ensures that atmospheric lithium abundance reflects core lithium content, and the observable lithium doublet thus acts as a gauge for the core temperature and contraction age. The so-called 'lithium edge' that separates objects with lithium from those without can be seen in co-eval populations (e.g. in open clusters and MGs), through the spectral type (or mass). The lithium edge advances towards later spectral type as a population ages (see Fig. 9 and caption of Paper I), and the presence or absence of lithium thus provides a critical age constraint as a function of an object's spectral type.

Due to the low resolution and the presence of artefacts in the Li I spectral region for sample B, we searched for the Li I doublet only in sample A candidates. The Li I region in the sample A spectra shows S/N values of no more than 10 in all the 12 candidates which hampers the search for the absorption line. We found the Li I absorption line in SIPS2045−6332 and SIPS2039−1126 only, but we do not discard the possibility of other fainter candidates with no signal in this region, presenting some absorption when better spectra can be achieved. We also measured Li I in LP944-20 with the parameters found here, obtaining logN(Li) = 3.00 ± 0.5 dex, using synthetic spectra with $T_{\rm eff}=2400$ K, log $g=4.0$, DUSTY atmosphere structure and a rotational velocity of 35 km s^{-1} (measured by us). This is within the uncertainties of other literature findings (see Section 4.4.1).

Clarke (2010) found the lithium signature in SIPS2045−6332 and SIPS2039−1126 suggesting youth and a BD nature inside the MG membership. Here, we obtained the theoretical Li I
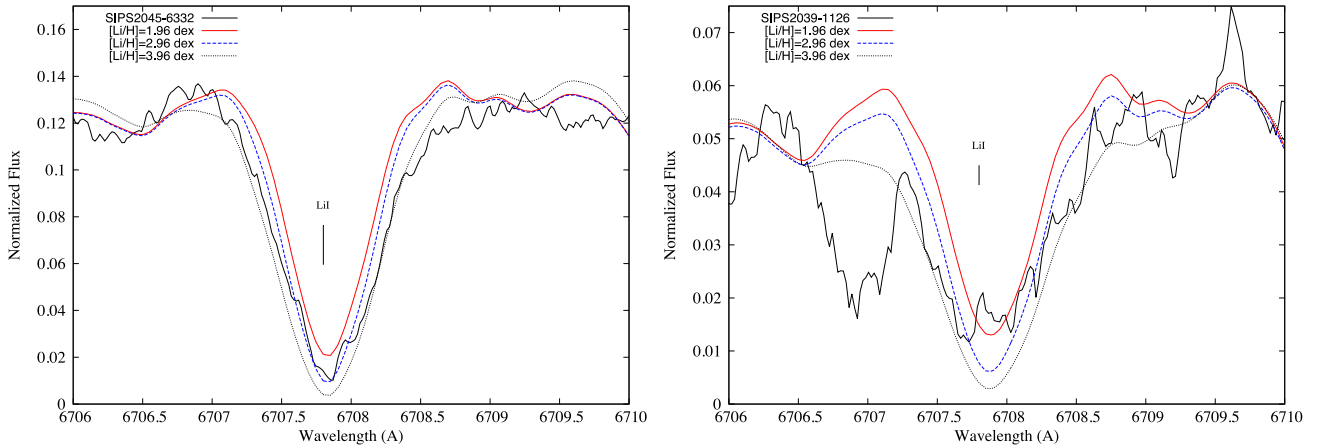
Figure 9. Fit to the observed spectra across Li ɪ resonance doublet for SIPS2045−6332 (left) and SIPS2039−1126 (right). Best synthetic fits are overplot with different Li abundances.

pseudo-equivalent widths, relative to the computed pseudo-continuum formed by molecular absorption, via direct integration of the line profile over the spectral interval 6703.0–6710.8Å. Fig. 9 shows the Li ɪ area for SIPS2045−6332 and SIPS2039−1126 with their respective fits. Li abundance of $\log N(\mathrm{Li}) = 3.5 \pm 0.5$ dex for SIPS2045−6332 and $\log N(\mathrm{Li}) = 3.0 \pm 0.5$ dex for SIPS2039−1126 provides age estimations as young as 7–100 Myr or the possible BD condition.

5.4 New brown dwarfs

The lithium test was first proposed by Rebolo, Martín & Maggazzú (1992) and developed by Magazzú, Martín & Rebolo (1993) to distinguish BDs from stellar objects. While stars and low-mass stars deplete lithium with time (see explanation in Section 5.3), substellar objects with $M < 0.06 \, M_\odot$ mass cannot achieve the temperature needed to destroy lithium and so it should be preserved independently of the object's age (Basri 2000; Chabrier & Baraffe 2000). Since young low-mass objects have not yet depleted all lithium, the discrimination between stars and BD through the lithium test should take age into account.

(i) **SIPS2045−6332:** SIPS2045−6332 was classified through several spectral indices as an M8.5 spectral type (Paper II). It shows a clear Li ɪ absorption line (Fig. 9). We used the parameters found in the best fit of the synthetic models and calculated its lithium abundance, $\log N(\mathrm{Li}) = 3.5 \pm 0.5$ dex. The DUSTY best-fitting $\log g$ values of 4.0 ± 0.5 and this lithium provide an age that confirms SIPS2045−6332 as probable Castor member.

We noticed that $EW(\mathrm{H}\alpha)$ value, 2.1, is quite small for a young object. But with a M8.5 spectral type, this value agrees with the findings of other authors, e.g. Mohanty & Basri (2003), Reiners & Basri (2010), Barnes et al. (2014), who found that the Hα emission is roughly constant from mid- to late M, but there is a sharp drop between M8 and L0 (see e.g. fig. 5 of Mohanty & Basri 2003), from which they show little or significantly reduced emission in spite of significant rotation.

At the Castor MG's age, and with a spectral type of M8.5 ($M < 0.06 \, M_\odot$), lithium confirms it also as a BD.

(ii) **SIPS2039−1126:** similarly, SIPS2039−1126 was classified through several spectral indices as an M8.0 spectral type (Paper II). It shows a Li ɪ absorption line (Fig. 9) although the S/N of the area is only ~5. Using the parameters from the best fit of the synthetic

models, we obtained $\log N(\mathrm{Li}) = 3.0 \pm 0.5$ dex (Section 5.3). The DUSTY best-fitting $\log g$ values of 4.5 ± 0.5 suggests it is probably still in contraction. In Section 5.1 we saw that $EW(\mathrm{Na}\,\textsc{i})$ of SIPS2039−1126 was high considering its Pleiades membership. We have used gravity criteria for targets up to 200 Myr but as seen in Fig. 6, following Schlieder et al. (2012), some Pleiades members may lie outside these limits. We thus cannot discard this target as a PL member taking into account the rest of the evidence.

At the Pleiades age or in the age interval suggested by the gravity values, the lithium depletion boundary occurs at M6.5 ($M = 0.075 \, M_\odot$; Barrado y Navascués et al. 2004). Thus, with an M8.0 spectral type, lithium confirms SIPS2039−1126 as a BD.

6 SUMMARY AND CONCLUSIONS

We have presented a study of the spectral signatures of 25 low-mass objects that were candidate members of five young MGs. We studied different typical age-constraining spectroscopic criteria utilizing high- and low-resolution spectra, and combined the results to extract a final membership assessment for each target.

We took into account spectral classification and thus approximated atmospheric temperature to apply the most appropriate model or models in the search of the best physical parameter constraints. When we used the synthetic stellar atmospheric models, the good agreement between observed and theoretical energy distributions suggests that semi-empirical models describe well the impact of dust in the atmospheres of M dwarfs. S-function analysis shows that the inclusion of dust effects makes it possible to achieve better fits for objects with $T_{\mathrm{eff}} \leq 2800$ K.

In both samples, although youth can generally be established, $\log g$ and $EW(\mathrm{Na}\,\textsc{i})$ were not useful for discriminating between different MGs. Some targets of sample A that were candidates to the HY MG having lower $\log g$ values than candidates to younger MGs, and similarly in $EW(\mathrm{Na}\,\textsc{i})$ values. In sample B the values are more consistent but most of the targets have several candidatures, making the situation more complicated. However, looking at the final membership results, only one target of sample A is classified as a member of a MG with age <200 Myr, which makes this criterion non-applicable for most of them. For sample B, in spite of the multiple membership candidatures in the final results, we can discriminate between the lower values of $\log g$ [or lower values of $EWs(\mathrm{Na}\,\textsc{i})$] for targets that are members of younger MGs, medium values for targets that are members of intermediate-age MGs and

the higher values for targets that are members of oldest MGs, which finally is consistent with the log *g*–age relation. The comparison of *EW*(Na I)s is probably useful to discriminate very young targets (less than 100 Myr) in a homogeneous sample (as suggested by Schlieder et al. 2012) while log *g* values are probably useful to discriminate very young (less than 100 Myr) and very old (more that 600 Myr) objects, serving as complementary study to other criteria.

The activity-age relation is a reasonably useful age criterion up to ≈*M*7 spectral type but activity variability, binarity, and the comparison of different instruments/resolution can introduce considerable uncertainties in age estimation. The presence of Lithium discriminates between young and old low-mass stars but an ambiguity between young low-mass stars and BDs limits its use in this cool temperature region. Gravity-sensitive features and rotational velocity can be useful youth indicators in support of activity and lithium diagnostics, but clearly have large dispersion and they need to be applied in conjunction with similar data. For a reliable constraint of cool object ages, a combination of different criteria are needed.

We find 10 of the 13 objects from sample A to be probable members of one of the MGs, and also that 2MASS0020−2346 is a young disc member. SIPS0007−2458, a candidate member of the IC2391 MG, shows positive candidature under most criteria but does not show the expected lithium (associated with the age of the IC2391 MG). Due to the age constraint from Hα emission and surface gravity, we are inclined to think that SIPS0007−2458 is probably a young object from the YD class, but is not in the IC2391 MG, although it could also be a contaminant field object. 2MASS0334−2130 is a similar case, with an M4.5-6 spectral type, it should contain lithium if it were an IC2391 MG member. Except for the Hα criterion, that could be reflecting a maximum in activity level or the influence of an unseen companion, everything indicates that 2MASS0334−2130 is older than the IC2391 MG. Thus we also conclude that 2MASS0334−2130 is not an IC2391 member, although it could be a young object from the YD, or a contaminant target from the field.

In sample B, 10 objects could be MG members, although more information is needed to discriminate between the possible MG membership of objects with several candidatures. We could not obtain any results for 2MASS1909−1937, so this remains an astrometric candidate to the Castor MG. 2MASS1734−1151 gave contradictory results so it also remains an astrometric Pleiades MG candidate until further analysis can be performed.

We also confirm two MG candidates, SIPS2045−6332 and SIPS2039−1126, as BDs.

With all the acquired information, we find that 85 per cent, 83 per cent and 84 per cent of samples A, B, and both combined show spectroscopic signatures of youth in agreement with the age of the MG to which they present kinematic membership. This result suggests that there is a fairly low rate of contamination in such kinematic candidate samples. Also, there are candidates that cannot be confirmed or dismissed with the information obtained, which might (in the future) increase the final confirmation rate. We note that additional diagnostics to assess membership may be measured in the future, such as chemical tagging. Recently, in a kinematical-chemical investigation of the AB Dor MG 'Stream, Barenfeld et al. (2013) show that kinematics, colour–magnitude positions, and stellar youth indicators alone can be insufficient for testing whether a kinematic group of stars actually shares a common origin. Future chemical study of our MG candidates will complement this study.

In addition, this study has also helped to test and improve the atmosphere models for cool dwarfs (see Kuznetsov et al. 2012; Kuznetsov, Pavlenko & Gálvez-Ortiz 2013). Youth can be an advantage for various reasons. Because young objects are brighter they can be detected and studied out to greater distance than older, fainter objects. Also, the proximity of the MGs can allow the exploration of the faint circumstellar environment at relatively small distances from the star. Indeed, we will target our strongest MG candidates to search for lower mass companions using high-resolution imaging techniques (e.g. adaptive optics). The discovery of planetary systems around young and low-mass objects provides crucial information for the understanding of planetary and stellar formation.

From our complete study of the 80 objects considered (within Papers I, II and this paper), we have found a total of 45 new possible MG members (with eight of them showing more than one MG candidature) and around 21 possible young disc objects with no clear membership of the five MGs considered.

Of these we find 26, 13, 6, 4 and 5 possible members of the Hyades, Castor, Ursa Major, Pleiades and IC2391 MGs, respectively. Tables A1 and A2 of the appendix compile all the M-L dwarfs investigated in our study.

ACKNOWLEDGEMENTS

REFERENCES

Allard F., Hauschildt P. H., Alexander D. R., Tamanai A., Schweitzer A., 2001, ApJ, 556, 357

Allard N. F., Allard F., Hauschildt P. H., Kielkopf J. F., Machin L., 2003, A&A, 411, 473

Allard F., Homeier D., Freytag B., 2011, ASP Conf. Ser. Vol. 448, Model Atmospheres From Very Low Mass Stars to Brown Dwarfs. Astron. Soc. Pac., San Francisco, p. 91

Anders E., Grevesse N., 1989, Geochim. Cosmochim. Acta, 53, 3273

Antoja T., Figueras F., Fernández D., Torra J., 2008, A&A, 490, 135

Barenfeld S. A., Bubar E. J., Mamajek E. E., Young P. A., 2013, ApJ, 766, 6B

Barnes J. R. et al., 2014, MNRAS, preprint (arXiv:1401.5350)

Barrado y Navascués D., 2006, A&A, 459, 511

Barrado y Navascués D., Stauffer J. R., Jayawardhana R., 2004, AJ, 614, 386

Basri G., 2000, ARA&A, 38, 485
Basri G., Laurant R., Walter F. M., 1985, ApJ, 298, 761
Basri G., Mohanty S., Allard F., Hauschildt P. H., Delfosse X., Martín E. L., Forveille T., Goldman B., 2000, ApJ, 538, 363
Berger E. et al., 2008, ApJ, 676, 1307
Bovy J., Hogg D. W., 2010, ApJ, 717, 617
Burrows A., Volobuyev M., 2003, ApJ, 583, 985B
Burrows A., Hubbard W. B., Lunine J. I., Liebert J., 2001, Rev. Mod. Phys., 73, 719
Chabrier G., Baraffe I., 2000, ARA&A, 38, 337
Clarke J. R. A., 2010, PhD thesis, University of Hertfordshire
Clarke J. R. A. et al., 2010, MNRAS, 402, 575 (Paper I)
Correia A. C. M. et al., 2010, A&A, 511, A21
Cruz K. L., Reid I. N., 2002, AJ, 123, 2828
Dahn C. C. et al., 2002, AJ, 124, 1170
Deacon N. R., Hambly N. C., 2007, A&A, 468, 163
Deacon N. R., Hambly N. C., Cooke J. A., 2005, A&A, 435, 363
Eggen O. J., 1984a, AJ, 89, 1358
Eggen O. J., 1984b, ApJS, 55, 597
Eggen O. J., 1989, PASP, 101, 366
Famaey B., Pont F., Luri X., Udry S., Mayor M., Jorissen A., 2007, A&A, 461, 957
Famaey B., Siebert A., Jorissen A., 2008, A&A, 483, 453
Folkes S. L., 2009, PhD thesis, University of Hertfordshire
Folkes S. L. et al., 2012, MNRAS, 427, 3280
Francis C., Anderson E., 2009, RSPSA, 465, 3425
Gálvez-Ortiz M. C., 2005, PhD thesis, Universidad Complutense de Madrid
Gálvez-Ortiz M. C. et al., 2010, MNRAS, 409, 552 (Paper II)
Gorlova N. I., Meyer M. R., Rieke G. H., Liebert J., 2003, ApJ, 593, 1074
Gray D. F., 2005, The Observation and Analysis of Stellar Photospheres. Cambridge Univ. Press, New York
Hauschildt P., Allard F., 1992, ApJ, 512, 377
Jenkins J. S., Ramsey L. W., Jones H. R. A., Pavlenko Y., Gallardo J., Barnes J. R., Pinfield D. J., 2009, ApJ, 704, 975
Jones H. R. A., Tsuji T., 1997, ApJ, 480, 1400
Jones H. R. A., Longmore A. J., Allard F., Hauschildt P. H., 1996, MNRAS, 280, 77
Kirkpatrick J. D., Kelly D. M., Rieke G. H., Liebert J., Allard F., Wehrse R., 1993, ApJ, 402, 643
Kirkpatrick J. D., Henry T. J., Simons D. A., 1995, AJ, 109, 797
Klement R., Fuchs B., Rix H. W., 2008, ApJ, 685, 261
Kupka F., Piskunov N., Ryabchikova T. A., Stempels H. C., Weiss W. W., 1999, A&AS, 138, 119
Kuznetsov M. K., Pavlenko Ya. V., Gálvez-Ortiz M. C., 2012, Kinematics Phys. Celestial Bodies (KPCB) J., 28, 280
Kuznetsov M. K., Pavlenko Ya. V., Gálvez-Ortiz M. C., 2013, EPJ Web Conf., 47, 04002
López-Santiago J., 2005, PhD thesis, Universidad Complutense de Madrid
López-Santiago J., Micela G., Montes D., 2009, A&A, 499, 129
Luhman K. L., Liebert J., Rieke G. H., 1997, ApJ, 489, L165
Luyten W. J., 1978, IAU Symp. 80, 63
Lyubchik Yu., Pavlenko Ya., 2000, KFNT Suppl. 3, 360
Magazzù A., Martín E. L., Rebolo R., 1993, ApJ, 404, L17
Marcy G. W., Butler R. P., Vogt S. S., Fischer D. A., Lissauer J. J., 1998, ApJ, 505, L147
Martín E. L., Rebolo R., Zapatero Osorio M. R., 1996, ApJ, 469, 706
Martín E. L., Delfosse X., Basri G., Goldman B., Forveille T., Zapatero Osorio M. R., 1999, AJ, 118, 2466
Martín E. L. et al., 2010, A&A, 517, A53
Martínez-Arnáiz R., López-Santiago J., Crespo-Chacón I., Montes D., 2011, MNRAS, 414, 2629
McGovern M. R., Kirkpatrick J. D., McLean I. S., Burgasser A. J., Prato L., Lowrance P. J., 2004, AJ, 600, 1020
Mochnacki S. W. et al., 2002, AJ, 124, 2868
Mohanty S., Basri G., 2003, AJ, 583, 451
Murgas F., Jenkins J. S., Rojo P., Jones H. R. A., Pinfield D. J., 2013, A&A, 552, 27
Pavlenko Ya. V., 1997, Ap&SS, 253, 43
Pavlenko Ya. V., Jones H. R. A., Martín E. L., Guenther E., Kenworthy M. A., Zapatero Osorio M. R., 2007, MNRAS, 380, 1285
Pinfield D. J., Jones H. R. A., Lucas P. W., Kendall T. R., Folkes S. L., Day-Jones A. C., Chappelle R. J., Steele I. A., 2006, MNRAS, 368, 1281
Pizzolato N., Maggio A., Micela G., Sciortino S., Ventura P., 2003, A&A, 397, 147
Plez B., 1998, A&A, 337, 495
Pokorny R. S., Jones H. R. A., Hambly N. C., 2003, A&A, 397, 575
Pokorny R. S., Jones H. R. A., Hambly N. C., Pinfield D. J., 2004, A&A, 421, 763
Rajpurohit A. S., Reyle C., Schultheis M., Leinert C., Allard F., 2011, in Alecian G., Belkacem K., Samadi R., Valls-Gabaud D., eds, SF2A-2011: Proceedings of the Annual Meeting of the French Society of Astronomy and Astrophysics, p. 339
Rajpurohit A. S., Reylé C., Schultheis M., Allard F., Scholz R., Homeier D., 2012, in Boissier S., de Laverny P., Nardetto N., Samadi R., Valls-Gabaud D., Wozniak H., eds, SF2A-2012: Proceedings of the Annual meeting of the French Society of Astronomy and Astrophysics. p. 383
Rebolo R., Martín E. L., Magazzú A., 1992, ApJ, 389, L83
Rebolo R., Martín E. L., Basri G., Marcy G. W., Zapatero-Osorio M. R., 1996, ApJ, 469, L53
Reiners A., Basri G., 2008, AJ, 684, 1390
Reiners A., Basri G., 2010, ApJ, 710, 924
Reylé C., Rajpurohit A. S., Schultheis M., Allard F., 2011, ASP Conf. Ser. Vol. 448, The Effective Temperature Scale of M Dwarfs from Spectral Synthesis. Astron. Soc. Pac., San Francisco, p. 929
Ribas I., 2003, A&A, 400, 297
Rutten R. G. M., 1987, A&AS, 177, 131
Ryan R. D., Neukirch T., Jardine M., 2005, A&A, 433, 323
Schlieder J. E., Lépine S., Rice E., Simon M., Fielding D., Tomasino R., 2012, AJ, 143, 114S
Schrijver C. J., Zwaan C., 1991, A&AS, 251, 183
Shanklad P. D. et al., 2006, ApJ, 653, 700
Shkolnik E., Liu M. C., Reid I. N., 2009, ApJ, 699, 649S
Silvestri N. M. et al., 2006, AJ, 131, 1674
Skumanich A., 1972, ApJ, 491, 856
Stauffer J. R., Liebert J., Giampapa M., 1995, AJ, 109, 298
Stauffer J. R., Balachandran S. C., Krishnamurthi A., Pinsonneault M., Terndrup D. M., Stern R. A., 1997, ApJ, 475, 604
Terndrup D. M., Stauffer J. R., Pinsonneault M. H., Sills A., Yuan Y., Jones B. F., Fischer D., Krishnamurthi A., 2000, AJ, 119, 1303
Tinney C. G., 1998, MNRAS, 296, L42
Tsuji T., Ohnaka K., Aoki W., 1996, A&AS, 305, L1
West A. A. et al., 2004, AJ, 128, 426
West A. A., Hawley S. L., Bochanski J. J., Covey K. R., Reid I. N., Dhital S., Hilton E. J., Masuda M., 2008, AJ, 135, 785
West A. A. et al., 2011, AJ, 141, 97
Zapatero Osorio M. R., Béjar V. J. S., Pavlenko Ya., Rebolo R., Allende Prieto C., Martín E. L., García López R. J., 2002, A&A, 384, 937
Zhao J., Zhao G., Chen Y., 2009, ApJ, 692, L113

APPENDIX A: TABLES

Table A1. Compilation of all VLM MG candidates: the fifth column describes the method or methods from which membership has been derived. When the word probable is used we mean that kinematics is not supported by $v \sin i$ criterion of Paper II. Spectral types given are from spectral indices (calculated in Paper II and here) except when marked.

Name	α (2000) (h m s)	δ (2000) (° ′ ″)	*SpT*	Note
Hyades				
SIPS0004−5721	0 4 18.970	−57 21 23.30	M7.0	Also IC candidate; kinematic
SIPS0027−5401	0 27 23.240	−54 1 46.20	M6.0	Kinematics + age features
2MASS0123−3610	1 23 0.506	−36 10 30.67	M4.5	Kinematics
SIPS0153−5122	1 53 11.430	−51 22 24.99	M6.0	Kinematics + age features
SIPS0214−3237	2 14 45.440	−32 37 58.20	M6.5	Kinematics + age features
SIPS0235−0711	2 35 49.470	−7 11 21.90	M6.0	Kinematics + age features
SIPS0440−0530	4 40 23.328	−5 30 7.85	M7.5	Kinematics
2MASS0600−3314	6 0 33.750	−33 14 26.84	M7.0^{phot}	Probable member from kinematics
2MASS0814−4020	8 14 35.46	−40 20 49.26	M7-8	Photometry + astrometry + age features
2MASS1745−1640	17 45 34.66	−16 40 53.81	M9-L2	Also CA and SI candidate; photometry + astrometry + age features
SIPS2014−2016	20 14 3.523	−20 16 21.30	M7.5	Kinematics
2MASS2031−5041	20 31 27.495	−50 41 13.49	M5.0	Kinematics
SIPS2049−1716	20 49 52.610	−17 16 7.80	M6.5	Kinematics
SIPS2100−6255	21 0 30.227	−62 55 7.31	M5.0^{phot}	Kinematics
DENIS2200−3038	22 0 2.022	−30 38 32.71	M9.0	Probable member from kinematics
SIPS2200−2756	22 0 16.838	−27 56 29.70	M6.0	Probable member from kinematics
2MASS2207−6917	22 7 10.313	−69 17 14.25	M6.5	Kinematics
2MASS2231−4443	22 31 8.657	−44 43 18.43	M4.5	Kinematics
LEHPM4908	22 36 42.656	−69 34 59.30	M5.5	Kinematics + age features
2MASS2311−5256	23 11 30.330	−52 56 30.17	M5.5	Kinematics
SIPS2318−4919	23 18 45.952	−49 19 17.79	M6.5	Kinematics
SIPS2322−6357	23 22 5.332	−63 57 57.60	M6.5	Kinematics
SIPS2347−1821	23 47 16.662	−18 21 50.60	M6.5	Kinematics
SIPS2350−6915	23 50 3.948	−69 15 24.39	M6.5	Kinematics
LEHPM6375	23 52 49.138	−22 49 29.54	M6.5	Probable member from kinematics
LEHPM6542	23 57 54.822	−19 55 1.89	M6.0	Kinematics + age features
Ursa Major				
2MASS1146−4754	11 46 51.04	−47 54 38.17	M7-8	Photometry + astrometry + age features
2MASS1236−6536	12 36 32.38	−65 36 35.6	M4.0	Also CA candidate; photometry + astrometry + age features
2MASS1433−5148	14 33 41.95	−51 48 03.70	M6-7	Also CA candidate; photometry + astrometry + age features
2MASS1618−3214	16 18 08.92	−32 14 36.17	M6.5	Also CA candidate; photometry + astrometry + age features
2MASS1736−0407	17 36 56.09	− 4 07 25.84	M4-5	Also CA candidate; photometry + astrometry + age features
2MASS1745−1640	17 45 34.66	−16 40 53.81	M9-L2	Also HY and CA candidate; photometry + astrometry + age features
Castor				
DENIS0021−4244	0 21 5.896	−42 44 43.33	M9.5	Kinematics + age features
2MASS1236−6536	12 36 32.38	−65 36 35.6	M4.0	Also SI candidate; photometry + astrometry + age features
2MASS1433−5148	14 33 41.95	−51 48 03.70	M6-7	Also SI candidate; photometry + astrometry + age features
2MASS1618−3214	16 18 08.92	−32 14 36.17	M6.5	Also SI candidate; photometry + astrometry + age features
2MASS1736−0407	17 36 56.09	− 4 07 25.84	M4-5	Also SI candidate; photometry + astrometry + age features
2MASS1745−1640	17 45 34.66	−16 40 53.81	M9-L2	Also HY and SI candidate; photometry + astrometry + age features
2MASS1756−4518	17 56 29.63	−45 18 22.47	M8-9	Photometry + astrometry + age features
2MASS1909−1937	19 09 08.21	−19 37 47.96	L0.0	Photometry + astrometry
SIPS2000−7523	20 0 48.171	−75 23 6.58	M8.0	Probable member from kinematics
SIPS2045−6332	20 45 2.278	−63 32 5.30	M9.0	Kinematics + age features
SIPS2114−4339	21 14 40.928	−43 39 51.20	M6.5	Kinematics
2MASS2242−2659	22 42 41.294	−26 59 27.23	M5.5	Also HY candidate; kinematics
2MASS2254−3228	22 54 58.110	−32 28 52.20	M5.5	Kinematics + age features
Pleiades				
2MASS1557−4350	15 57 27.39	−43 50 21.47	M7.5-8.5	Also IC candidate; photometry + astrometry + age features
2MASS1734−1151	17 34 30.53	−11 51 38.83	M9.0	Photometry + astrometry
SIPS2039−1126	20 39 13.081	−11 26 52.30	M7.0	Kinematics + age features
HB2124-4228	21 27 26.133	−42 15 18.39	M7.5	Kinematics
IC 2391				
SIPS0004−5721	0 4 18.970	−57 21 23.30	M7.0	Also HY candidate; kinematics

Table A1 – *continued*

Name	α (2000) (h m s)	δ (2000) (° ′ ″)	*SpT*	Note
2MASS1326−5022	13 26 53.48	−50 22 27.04	M7.5	Photometry + astrometry + age features
2MASS1557−4350	15 57 27.39	−43 50 21.47	M7.5-8.5	Also PL candidate; photometry + astrometry + age features
2MASS1618−3214	16 18 08.92	−32 14 36.17	M6.5	Also CA and SI candidate; photometry + astrometry + age features
SIPS2341−3550	23 41 47.497	−35 50 14.40	M7.0	Kinematics

Table A2. Other probably young disc and old disc candidates. Notes as in previous table.

Name	α (2000) (h m s)	δ (2000) (° ′ ″)	*SpT*	Note
Other young disc				
SIPS0007−2458	0 7 7.800	−24 58 3.80	M7.5	Kinematics + age features
2MASS0020−2346	0 20 23.155	−23 46 5.38	M6.0	Kinematics + age features
SIPS0039−2256	0 39 23.250	−22 56 44.90	M7.5	Probable YD from kinematics
DENIS0041−5621	0 41 35.390	−56 21 12.77	M7.5	Kinematics
SIPS0054−4142	0 54 35.300	−41 42 6.20	M5.0	Probable YD from kinematics
SIPS0109−0343	1 9 51.040	−3 43 26.30	M9.0	Not conclusive from kinematics
LEHPM1289	1 9 59.579	−24 16 47.82	M6.0	Not conclusive from kinematics
SIPS0115−2715	1 15 26.610	−27 15 54.10	M5.0	Not conclusive from kinematics
SIPS0126−1946	1 26 49.980	−19 46 5.90	M6.0	Not conclusive from kinematics
LEHPM1563	1 27 31.956	−31 40 3.18	M8.5	Kinematics
SIPS0212−6049	2 12 33.580	−60 49 18.40	M6.5	Not conclusive from kinematics
2MASS0334−2130	3 34 10.657	−21 30 34.35	M4.5	Kinematics + age features
2MASS0429−3123	4 29 18.426	−31 23 56.81	M7.5	Not conclusive from kinematics
2MASS0502−3227	5 2 38.677	−32 27 50.07	M5.5	Not conclusive from kinematics
2MASS0528−5919	5 28 5.623	−59 19 47.17	M5.5	Not conclusive from kinematics
SIPS1039−4110	10 39 18.340	−41 10 32.00	M6.5$^{\text{phot}}$	Probable YD from kinematics
SIPS1124−2019	11 24 22.229	−20 19 1.50	M7.0$^{\text{phot}}$	Probable YD from kinematics
SIPS2049−1944	20 49 19.673	−19 44 31.30	M7.0	Kinematics
SIPS2128−3254	21 28 17.402	−32 54 3.90	M6.5	Kinematics
SIPS2321−6106	23 21 43.418	−61 6 35.37	M5.0	Kinematics
SIPS2343−2947	23 43 34.731	−29 47 9.50	M8.0	Kinematics
Old Disc				
2MASS0204−3945	2 4 18.036	−39 45 6.48	M7.0	Not conclusive from kinematics
2MASS0445−5321	4 45 43.368	−53 21 34.56	M7.5$^{\text{phot}}$	Kinematics
DENIS1250−2121	12 50 52.654	−21 21 13.67	M7.5	Kinematics
SIPS1329−4147	13 29 0.872	−41 47 11.90	M9.5$^{\text{phot}}$	Kinematics
SIPS1341−3052	13 41 11.561	−30 52 49.60	L0$^{\text{phot}}$	Kinematics
2MASS1507−2000	15 7 27.799	−20 0 43.18	M7.5	Kinematics
SIPS1632−0631	16 32 58.799	−6 31 45.30	M8.5	Kinematics
SIPS1758−6811	17 58 59.663	−68 11 10.50	M5.0	Probable OD from kinematics
SIPS1949−7136	19 49 45.527	−71 36 50.89	M7.0	Kinematics
2MASS2001−5949	20 1 24.639	−59 49 0.09	M6.0	Probable OD from kinematics
2MASS2106−4044	21 6 20.896	−40 44 51.91	M6.0	Probable OD from kinematics
SIPS2119−0740	21 19 17.571	−7 40 52.50	M7.0	Probable OD from kinematics
LEHPM4480	22 15 10.151	−67 38 49.07	M5.5	Probable OD from kinematics
2MASS2222−4919	22 22 3.684	−49 19 23.45	M6.5	Kinematics

This paper has been typeset from a TEX/LATEX file prepared by the author.